INVESTIGATION OF GAS SENSING PROPERTIES OF NANOPARTICLES FUNCTIONALIZED WITH FERROCENE MOLECULES

A Thesis Submitted to
the Graduate School of Engineering and Sciences of
İzmir Institute of Technology
in Partial Fulfillment of the Requirements for the Degree of

MASTER OF SCIENCE

in Materials Science and Engineering

by
Abdurrahman Halis GÜZELAYDIN

December 2013
İZMİR

We approve the thesis of **Abdurrahman Halis GÜZELAYDIN**

Examining Committee Members:

_____

Assist. Prof. Dr. Enver TARHAN
Department of Physics, İzmir Institute of Technology

_____

Prof. Dr. Salih OKUR
Department of Materials Science and Engineering, İzmir Katip Çelebi University

_____

Prof. Dr. Orhan ÖZTÜRK
Department of Physics, İzmir Institute of Technology

_____

Assoc. Prof. Dr. Mustafa M. DEMİR
Department of Materials Science and Engineering, İzmir Institute of Technology

_____

Assist. Prof. Dr. Ömer MERMER
Department of Electrical-Electronics Engineering, Gediz University

16 December 2013

_____

Assist. Prof. Dr. Enver TARHAN
Supervisor, Department of Physics,
İzmir Institute of Technology

_____

Prof. Dr. Salih OKUR
Co-Supervisor, Department of
Materials Science and Engineering,
İzmir Katip Çelebi University

_____

Assoc. Prof. Dr. Mustafa M. DEMİR
Head of the Department of
Materials Science and Engineering

_____

Prof. Dr. R. Tuğrul SENGER
Dean of the Graduate School of
Engineering and Sciences

ACKNOWLEDGEMENTS

I would like to express my gratitude to my co-advisor Prof. Dr. Salih Okur and my advisor Assist. Prof. Dr. Enver Tarhan for their invaluable advice, guidance, and encouragement throughout this study.

I would like to thank Assist. Prof. Dr. Mehmet Şenel from Fatih University for supplying the materials used in this study. I would like to thank Assist. Prof. Dr. Mustafa Can from İzmir Katip Çelebi University for the insightful talks we made.

I would like to thank Center for Materials Research staff at İzmir Institute of Technology for their help and support during the characterization part of my study.

I would also like to thank my friends Abdullah Bayram, Cebrail Özbek and Cem Baytöre for their encouragement, help and patience all along.

And last but not least, I am also grateful to my family for leading me to this stage and for their endless support during all of my life.

ABSTRACT

INVESTIGATION OF GAS SENSING PROPERTIES OF NANOPARTICLES FUNCTIONALIZED WITH FERROCENE MOLECULES

In this study, gas sensing properties of ferrocene functionalized multi-wall carbon nanotubes (MWCNT) and iron oxide nanoparticles were investigated via acoustic wave and electrical based techniques. Commercially obtained multi-wall carbon nanotubes having amine functional groups grafted directly onto their surfaces were covalently functionalized with ferrocene molecules. Iron oxide nanoparticles synthesized by the alkaline coprecipitation of ferric and ferrous salts were functionalized with ferrocene molecules. Dispersions of each modified nanoparticle in 3 mL ethanol were prepared and sonicated for 12 h in order to ensure adequate homogeneity. 5 μL from each of these dispersions were then drop-cast onto AT-cut gold coated quartz crystal microbalance (QCM) and gold interdigitated (IDE) glass electrodes with 3 μm interdigit spacing followed by drying on hotplate at 60 °C for 30 min to deposit thin-films. The thin-film coated electrodes were exposed to alternately varying concentration levels of CO, CO_2, O_2 and humidity ranging from 0 vol% to 100 vol% in predetermined intervals by a computer controlled mass flow meter array in an electromagnetically shielded and hermetically sealed measurement cell specifically designed to acquire QCM and electrical signals from the electrodes. Gas sensor responses of the thin-film coated QCM electrodes were assessed by measuring the frequency shift of the vibrating quartz crystal from its natural resonance frequency and evaluating that value into adsorbed mass according to Sauerbrey relation, whereas, responses from the interdigitated electrodes were assessed by measuring the resistance changes through the thin-film coating under a compliance current value of 1.0000 mA.

ÖZET

FERROSEN MOLEKÜLLERİ İLE FONKSİYONEL HALE GETİRİLMİŞ NANOPARÇACIKLARIN GAZ SENSÖR ÖZELLİKLERİNİN İNCELENMESİ

Bu çalışmada, ferrosen molekülleri ile fonksiyonelleştirilmiş çok-duvarlı karbon nanotüplerin (ÇDKNT) ve demir oksit nanopartiküllerinin gaz algılama özellikleri akustik dalga ve elektriksel ölçüm tabanlı teknikler ile incelenmiştir. Ticari olarak temin edilen yüzeyine doğrudan amin grupları bağlı çok-duvarlı karbon nanotüpler kovalent olarak ferrosen molekülleri ile fonksiyonelleştirilmiştir. Fe^{3+} ve Fe^{2+} katyonları içeren tuzların alkali eşçökelmesi ile sentezlenen demir oksit nanopartikülleri ferrosen molekülleri ile fonksiyonelleştirilmiştir. Modifiye edilen her nanopartikülün 3 mL etanol içerisinde dispersiyonları hazırlanmış ve yeterli homojenliği sağlamak için ultrasonik banyoda 12 saat boyunca karıştırılmıştır. Sonrasında bu dispersiyonların her birinden 5μL alınarak, altın kaplı AT-kesim kuvars kristal mikroterazi (QCM) ve 3 μm tarak aralıklı altın birbirine geçmiş taraklı cam elektrotlar damlatma metodu ile kaplanıp, bunu takiben ince-film oluşumunu sağlamak üzere elektrotlar sıcak levha üzerinde 60 °C'de 30 dakika boyunca kurutulmuştur. İnce-film kaplı elektrotlar, bu elektrotlardan QCM ve elektriksel sinyalleri almak için özel olarak tasarlanmış elektromanyetik alan korumalı ve hermetik ölçüm hücresi içinde, bilgisayar kontrollü bir kütle akış metre dizisi aracılığı ile önceden belirlenen zaman aralıklarında hacmen %0 ve %100 arasında döngüsel olarak değişen konsantrasyon seviyelerinde CO, CO_2, O_2 ve neme maruz bırakılmıştır. İnce-film kaplı QCM elektrotların gaz duyarlılık tepkileri, titreşen kuvars kristalin doğal rezonans frekansındaki kayma ölçülüp, bu değer Sauerbrey bağıntısı uyarınca adsorplanan kütle hesaplanarak belirlenirken, birbirine geçmiş taraklı elektrotlardan alınan tepkiler ise 1.0000 mA limit akım değeri altında ince-film kaplamanın direncindeki değişimler ölçülerek belirlenmiştir.

TABLE OF CONTENTS

LIST OF FIGURES

Figure **Page**

LIST OF TABLES

Table **Page**

CHAPTER 1

INTRODUCTION

In today's ever developing society, high-technology has an immense impact in shaping the environment we are living in. Smart artifacts surrounding us became self-aware enough to make critical decisions otherwise necessitated human intervention. This is all possible, thanks to sensors, devices which selectively identify and measure physical, chemical, or biological parameters such as pressure, gas concentration, or the presence and concentration of a biological analyte (Zribi, 2009).

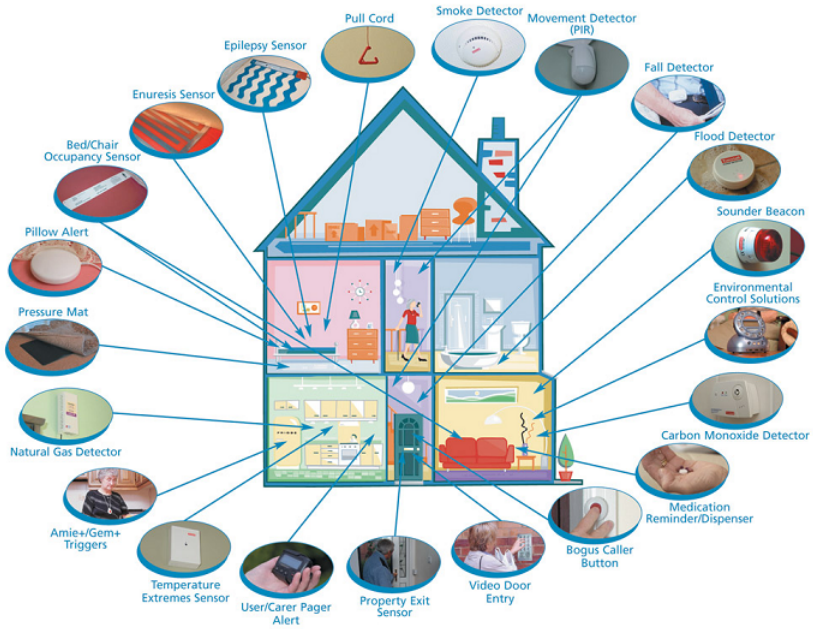

Figure 1.1. Various types of sensors utilized in a household environment.
(Source: Huber, 2005)

Amongst the sensor varieties, gas sensor technology has evolved tremendously over the past few decades and is becoming an indispensible technology. Due to increasing demands of reliable, inexpensive and portable systems for environmental monitoring, indoor air quality, food quality control, automotive, aerospace and many other applications, researchers are focusing their efforts utilizing novel ideas to develop

next-generation gas sensors to meet the necessary requirements, such as small size, low cost and power consumption for a functional gas sensor.

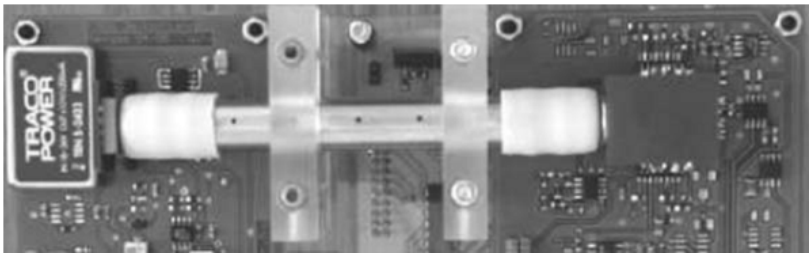

Figure 1.2. A state-of-the-art CO_2 gas-sensing micro-system hardware.
(Source: Spannhake et al., 2009)

In this respect; nanoscale science and technology, which is developing at a rapid pace, has a deep impact and pioneering role on every field of research that will dramatically change and revolutionize gas sensor technology. Due to their peculiar characteristics and size effects, nanomaterials such as nanowires, nanorods, nanotubes, nanoribbons, and nanoparticles often exhibit unusual physical properties that are different from those of their bulk counterparts, since the reduction in size introduces exceptional electrical, mechanical, chemical and optical properties which are largely believed to be the result of surface and quantum confinement effects. These mesoscopic materials are structures that are large compared to the atomic scale but rather small compared to the macroscopic scale, where carrier transport takes place in a manner that the Boltzmann equation is valid. Carriers do not exhibit fully wavelike behavior but are sufficiently delocalized to exhibit also some particle-like properties. The finite size of nanomaterials confines the electrons' wavefunctions, leading to quantized energy levels and a complete modification of the transport and optical properties of these materials. The extremely enhanced surface-volume ratio augments the role of the surface states in the sensor response. Sensing mechanisms controlled at the nanoscale level will therefore bring many benefits to the three "S" of sensor technology (sensitivity, selectivity, and stability). Consequently, these materials are of great interest both for fundamental study and for potential nanomaterial based gas sensor applications (Comini et al., 2009).

Among the new classes of nanomaterials, which draw a significant interest in solid-state chemical sensing applications, carbon nanotubes (CNTs) constitute a promising class of advanced nanomaterials with unprecedented electronic, chemical, structural, optical, mechanical and thermal properties for functional applications including nanodevices, nanoactuators and nanosensors.

A single-wall carbon nanotube (SWCNT) can be visualized as a graphene sheet rolled up into a hollow cylinder of a one-dimensional tubular wire with a diameter that ranges from about 0.5 nm to 5 nm and lengths on the order of micrometers to centimeters. A multi-wall carbon nanotube (MWCNT) is similar in structure to a single wall CNT but has multiple nested or concentric cylindrical walls with the spacing between walls comparable to the interlayer spacing in graphite, approximately 0.34 nm. The ends of a CNT are often capped with a hemisphere of the buckyball structure (Penza et al., 2005).

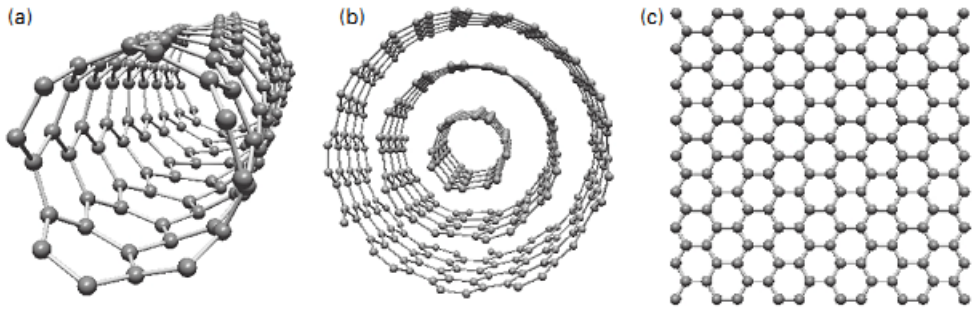

Figure 1.3. Ball-and-stick models of CNTs and graphene: (a) single-wall CNT, (b) multi-wall CNT with three shells, and (c) graphene, which is a single sheet of graphite.

Due to their peculiar hollow structure, nanosized morphology, high surface area (100-2000 m^2/g), high carrier mobility, high chemical reactivity at walls and mainly at caps, unlimited functionalization features, and excellent stability, carbon nanotubes are ideal candidates as highly sensitive gas sorption mediums. Advantages such as trace amount detection, fast response, high resolution, and specific chemical interactions between the surface carbon atoms and targeted gas molecules at room temperature render carbon nanotubes as attractive advanced functional nanomaterials to fabricate innovative high-performance gas sensors (Consales et al., 2006).

Again, in the context of the new classes of nanomaterials, nanoparticles are an exclusive class of advanced nanomaterials exhibiting a range of unique optical, chemical, and magnetic properties due to finite size effects. The most obvious difference between nanoparticles and larger colloids or bulk materials is their extremely high surface area. For any surface area limited interaction, this makes nanoparticles particularly interesting materials. A large quantity of energy is stored in nanoparticles as surface free energy, and this accumulated energy can mean increased reactivity, or altered optical, electronic, and magnetic properties. The surface atoms of nanoparticles are in a vastly different environment with respect to the atoms in a bulk material, and even compared to atoms in a thin-film material. Along with their exceptionally high surface area, due to their extreme curvature, nanoparticles have an enormous concentration of defect sites in crystals. So, confinement effects and surfaces that can be viewed as defective collectively have an impact on yielding the peculiar properties of the nanoparticles (Huber, 2005). All these facts demonstrate that specifically crafted nanoparticles are appealing sensitive nanomaterials for next-generation gas sensors.

Quartz crystal microbalance (QCM) is a versatile and established acoustic wave technique capable of sensitively detecting mass changes on the order of nanograms which is quite viable to observe adsorption and desorption of gas molecules with special thin-film coated QCM electrodes to study the gas sorption characteristics of the functional nanomaterials. Relying on the piezoelectric effect, QCM enables determination of minute amounts of mass variations as a function of the vibrational frequency shift of the QCM electrode from its natural resonance frequency due to adsorption and desorption of gas molecules on the thin-film coated quartz electrode.

Complimenting the acoustic wave technique, interdigitated electrodes (IDE) are used exploiting the room temperature conductivity of carbon nanotubes to observe the gas sensing process involving electronic charge transport and interactions of gas molecules with the conjugated electronic states of carbon nanotubes.

In the scope of this thesis, gas sensing properties of multi-wall carbon nanotubes and iron oxide nanoparticles, both modified with ferrocene molecules and unmodified, towards CO, CO_2, O_2 and humidity were investigated by means of acoustic wave and electrical based techniques. The thin-film coated electrodes were exposed to alternately varying concentration levels of CO, CO_2, O_2 and humidity ranging from 0 vol% to 100 vol% in predetermined intervals by a computer controlled mass flow meter array in an electromagnetically shielded and hermetically sealed measurement cell specifically designed to acquire QCM and electrical signals from the electrodes. Gas sensor responses of the thin-film coated QCM electrodes were assessed by measuring the frequency shift of the vibrating quartz crystal from its natural resonant frequency and evaluating that value into adsorbed mass according to Sauerbrey relation, whereas, responses from the interdigitated electrodes were assessed by measuring the resistance changes through the thin-film coating under a compliance current value of 1.0000 mA.

In Chapter 2 of this thesis, a literature survey on the main characteristics of gas sensors as well as the fundamental working principles of different types of gas sensors will be presented. In Chapter 3, the theory, method and materials employed throughout this study are detailed with references to prior literature works. The experimental procedure and the results of this study are given and discussed in Chapters 4 and 5, respectively, while the conclusions are stated in the last chapter.

CHAPTER 2

GAS SENSORS

2.1. Gas Sensors

A sensor is an analytical device that utilizes a responsive sensing layer to continuously and reversibly recognize a change in the parameters of a measured environment and convert this information into an analytically useful signal (Potyrailo, 2006).

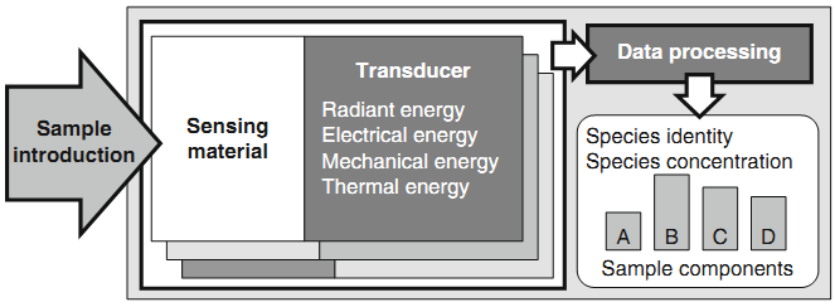

Figure 2.1. Main components of a sensor system.
(Source: Potyrailo, 2006)

As shown in Figure 2.1, in a device qualified as a chemical sensor, a sensing material is applied onto a suitable physical transducer to convert a change in a specific property of a sensing material into a suitable form of energy. The obtained signal from a single transducer or an array of transducers is further processed to provide useful information about the identity and concentration of species in the sample.

The energy transduction principles that have been employed for chemical sensing involve radiant, electrical, mechanical, and thermal types of energy. In Figure 2.2, gas sensing methods for chemical sensing applications are classified based on energy transduction principles.

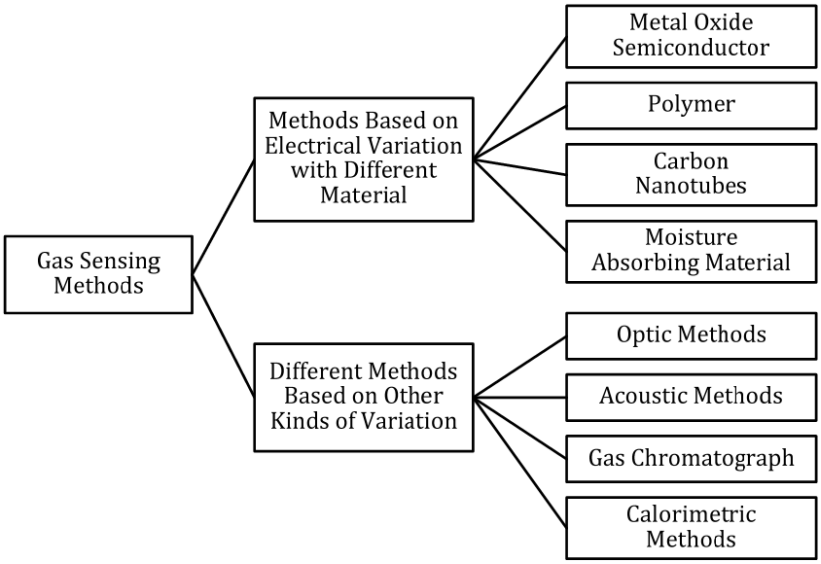

Figure 2.2. Classification of gas sensing methods.
(Source: Liu et al., 2012)

A further elaboration of the parameters associated with various energy transduction principles is presented in Table 2.1.

Table 2.1. Various quantities and their energy transduction principles employed by sensor systems.

Parameter	**Quantity**
Mechanical	Length, area, volume, velocity, acceleration, force, torque, pressure, sound wavelength, intensity, etc.
Thermal	Temperature, thermal gradient, entropy, etc.
Electrical	Voltage, current, resistance, charge, inductance, capacitance, dielectric constant, polarization, electric field, frequency, dipole moment, etc.
Optical	Intensity, phase shift, wavelength, polarization, index of refraction, etc.
Chemical	Concentration, reaction rate, pH, reduction/oxidation potentials, etc.
Magnetic	Flux density, magnetic moment, magnetic permeability, etc.

2.1.1. Requirements for an Ideal and Practical Sensor

The design of a sensor for a particular application will necessitate careful consideration of the nature and requirements of that application. Therefore, it is always practical to define the set of features for an ideal sensor that a specific application will demand to detect various chemical species. Ideally, the sensor should provide;

i. both adequate sensitivity (in some cases at the single-molecule level) and a broad dynamic range (the span of measurands),
ii. high selectivity towards the species of interest and immunity to sample-matrix interferences,
iii. multicomponent measurements,
iv. fast and reversible response, and excellent long-term stability,
v. robust, reliable, simple, economical, small size characteristics, and self-calibration capabilities (Potyrailo, 2006).

According to the aforementioned conditions, a list of performance attributes can be defined to assess sensor figures of merits (Zribi, 2009).

a. Accuracy: The maximum deviation of a transducer's output from the real value of the unknown measurand as determined by a calibration standard.
b. Precision: A measurement uncertainty associated with a transducer's probability of generating random errors. It quantifies statistical fluctuations in the measurement and is attributed to variabilities in the measurement conditions and the limitations of the selectivity of the sensor towards the measurand of interest. Precision represents the repeatability of the measurement given the same sample.

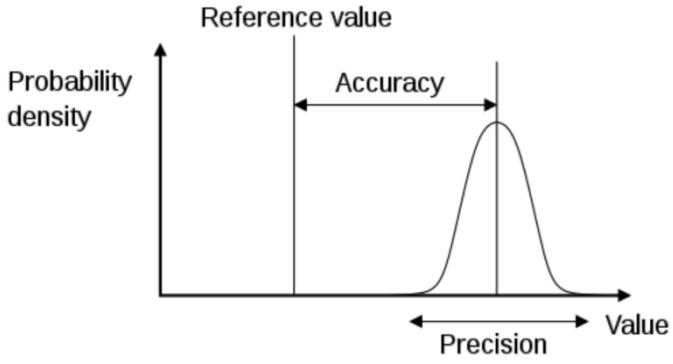

Figure 2.3. Graphical representations of accuracy and precision.

c. Resolution: The smallest change in the input of a transducer that leads to a detectable change in the output signal. Maximum resolution is attained at maximum sensitivity and minimum noise.
d. Sensitivity: The ratio of the signal generating quantity resulting from the energy transformations performed by the transducer to all the possible measurands and critical noise parameters that can affect the transducer sensitivity such as temperature and pressure.
e. Response Curve: Quantitative characteristic curve of a sensor that represents the output of the sensor versus the measurand applied to its input. The transducer response can be linear or nonlinear as shown in Figure 2.4.

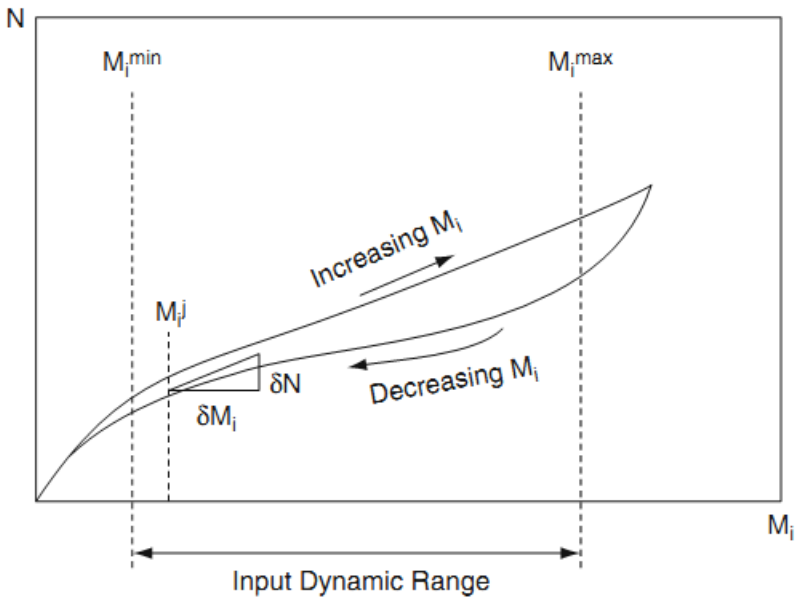

Figure 2.4. Typical response curve of a sensor/transducer *N* to a measurand M_i.

f. Input Dynamic Range: The span of measurands that constitute the overall operating domain for the device. Within this interval, the sensor is supposed to maintain its properties and reliability characteristics.
g. Selectivity: Tendency of a sensor designed to detect variations of a given measurand *M* to exhibit secondary internal sensitivities to other different measurands (M_i) or noise factors, physical or chemical, as well as biological in nature.

h. Response Time: The cumulative transient response of the sensor when it experiences a step change in the measurand incorporating the response times of the respective building blocks of the sensor.
i. Hysteresis and Drift: Hysteresis is the lagging of the sensor response behind the variation of the measurand. It can be attributed to sensing material's memory effect and/or to the transducer properties. As a performance specification, hysteresis is defined as the maximum difference between the upscale and downscale readings on the same artifact during a full-range traverse scan in each direction. It is often reported as the ratio (or percentage) of the difference between the upscale and downscale readings to the full scale. Drift is the slow unpredictable change of the sensor output at constant input. It can emanate from residual stress relaxation, residual diffusion, material aging, and degradation. It is defined for a specific time interval of interest.

2.2. Types of Gas Sensors

Solid-state gas sensors generate signals depending on changes in conductivity, capacitance, work function, mass, optical characteristics or energy exchanges due to solid/gas interactions at the transducer surface as a result of variations in concentrations of target gas molecules in an environment by using organic or inorganic functional materials as sensing elements. Basically, organic or inorganic (ex. conducting polymers, metal oxide semiconductors, etc.) materials are coated on the physical transducer surface of a device in the form of thick- or thin-films in order to create a gas sensitive active region. Signal acquisition is performed via conductive electrodes, diode and/or transistor structures, surface-wave components, thickness-mode transducers or optical apparatuses on the device. Despite measuring similar physical parameters, different transduction methods yielded different types of sensors utilizing alternative technologies. Types of solid-state gas sensors with their corresponding physical parameter changes used as gas detection principles are briefly listed in Table 2.2 (Capone et al., 2003).

Table 2.2. Types of solid state gas sensor devices with their corresponding physical parameter changes used as gas detection principles.

Device Type	Physical Parameter Change Used
Semiconductor gas sensors	Electrical conductivity
Field-effect gas sensors (diodes, transistors, capacitors)	Work function (electronic polarization)
Piezoelectric sensors (Quartz crystal microbalances (QCM), surface acoustic wave (SAW), micro-cantilevers)	Mass, surface perturbation
Optical sensors (fiber optic, thin-film)	Optical parameters: SPR, reflection, interferometry, absorption, fluorescence, refractive index or optical path length
Catalytic gas sensors (Seebeck effect, pellistors, semistors)	Reaction enthalpy or temperature
Electrochemical gas sensors (potentiometric or amperometric)	Electromotive force or electrical current in a solid-state electrochemical cell

2.2.1. Semiconductor Gas Sensors

Semiconductor gas sensors are metal oxide semiconductor based sensors which are normally high bandgap materials that are insulating in which the semiconducting behavior arises from stoichiometric deviations. Cation vacancies function as acceptors, producing holes, whereas oxygen vacancies act as donors since the bonding electrons in the adjacent cations are easily removed and donated to the conduction band.

$$O_o^X \Leftrightarrow \frac{1}{2}O_2 + V_O^{n+} + ne^- \tag{2.1}$$

Sensors based on metal oxide semiconductors are generally utilized to detect target gases through redox reactions between the target gases and the oxide surface. When the molecules of target gases react with the O^- distributed on oxide surface, it leads to an electronic variation of the oxide surface. Then, this variation is transduced

into an electrical resistance variation of the sensor. Metal oxide gas sensors are usually operated in air at elevated temperatures ranging between 200 and 500 °C, in order to increase the probability of gas molecule adsorption on the oxide surface and trigger the conductivity change of the sensing film where conduction is solely electronic in nature (Comini et al., 2009).

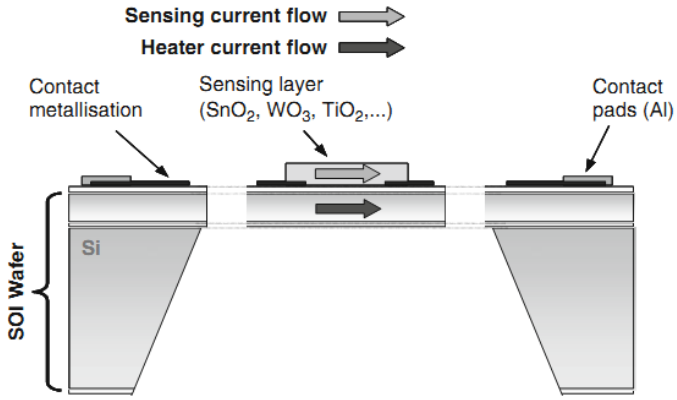

Figure 2.5. Cross-section of a metal oxide semiconductor based gas sensor.

2.2.2. Field-Effect Transistor (FET) Gas Sensors

The field-effect transistor is one of the most ubiquitous electronic components so they are very attractive candidates as transducers for chemical sensors. In a FET gas sensor, the gas species that react with the sensing layer induce a field effect, for example via adsorbing on the insulator surface forming, ex., -OH groups which have a large dipole moment, and therefore considerably influencing mobile charges in the semiconductor channel. Modulation of the shape and hence the conductivity of the channel gives rise to the sensor response (Salamonsson et al., 2005).

Among a variety of FET devices developed for specific purposes, MOSFETs are widely used in gas sensor applications. The basic MOSFET device contains the drain, source and gate terminals that are built on top of a SiO_2 insulating layer. The channel between the drain and source terminals is made up of a sensing material which exhibit a characteristic *I-V* curve depending on the gas concentration of the surrounding environment.

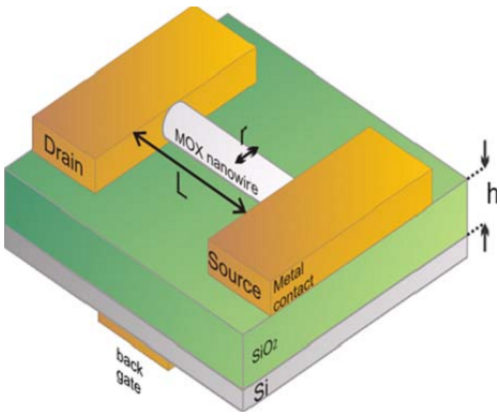

Figure 2.6. Layout of a single nanowire MOSFET with a metal oxide nanowire acting as channel. (Source: Comini et al., 2009)

2.2.3. Optical Gas Sensors

Spectroscopic methods such as ellipsometry, interferometry, surface plasmon resonance (SPR) are used for chemical detection and biosensor applications. Optical sensors using spectroscopic techniques fundamentally monitor the absorption/emission /scattering of a gaseous measurand at defined optical wavelengths. The wavelength distribution of a selected optical emission source enables identification of the presence of a specific gas species, while the intensity of absorption/emission/ scattering provides concentration data. Thus, spectroscopic optical methods are fast, accurate and stable measurement techniques for gas species having significant absorption or emission of optical radiation at a definite wavelength. In most cases they offer high gas sensitivity (on the order of parts per billion - ppb - or better), selectivity, and real-time continuous measurement capability. Many gases of interest (like CH_4, CO, CO_2, HF, HCl, H_2S, NO, N_2O, NH_3, SF_6, etc.) exhibit absorption in the infrared and near-infrared regions of the spectrum with the strength of the absorption at a particular wavelength corresponding to the concentration of the gas.

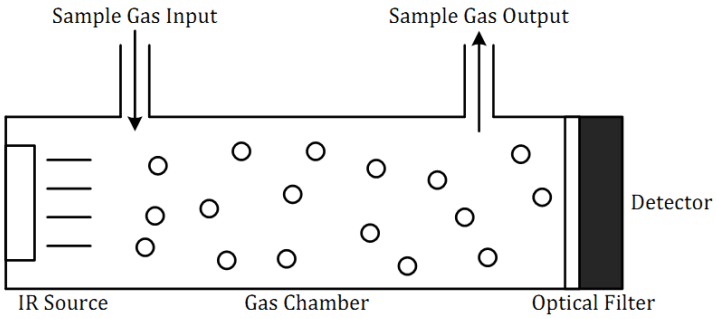

Figure 2.7. Schematic view of an infrared (IR) source gas sensor based-on absorption spectrometry. (Source: Liu et al., 2012)

2.2.4. Electrochemical Gas Sensors

Electrochemical gas sensors are based on measurement of the current (amperometric), voltage (potentiometric) or conductivity across the electrodes resulting from chemical reactions between the target gas molecules and the sensing electrode. Gas molecules permeating through a hydrophobic membrane initiates oxidation-reduction reactions with the active electrode. Current or voltage depending on gas concentration is acquired through an external circuit connected to the electrodes. An example redox reaction couple which takes place in an electrochemical carbon monoxide sensor is given below.

$$CO + H_2O \rightarrow CO_2 + 2H^+ + 2e^-$$

$$O_2 + 4H^+ + 4e^- \rightarrow 2H_2O \qquad (2.2.2)$$

There are generally two electrodes in an electrochemical sensor cell, one which is referred to as the active sensing electrode where the chemical reactions take place. In order to measure the electrochemical potential of the electrolyte and the electrode, a third electrode can be used as a reference electrode. This reference electrode is used to correct errors caused by the working electrode. The active electrode is made of noble metals or materials which are coated with platinum, palladium, carbon. To obtain a measurable signal, electrodes must have sufficiently large surface areas in contact with the analyte. The electrode materials specifically developed for the gas of interest catalyses reactions. A current that is proportional to the gas concentration flows

between the anode and the cathode with the aid of a resistor connected across the electrodes. Due to the fact that the power consumption of electrochemical sensors is the lowest among all sensor types available for gas monitoring, these sensors are widely used in portable instruments that contain multiple sensors. The cell can measure the electrical signals as current, potential, conductivity or capacitance.

Electrochemical gas sensors are widely used at homes and industries because they are simple, inexpensive and have high sensitivity to gas molecules (Chou, 2000).

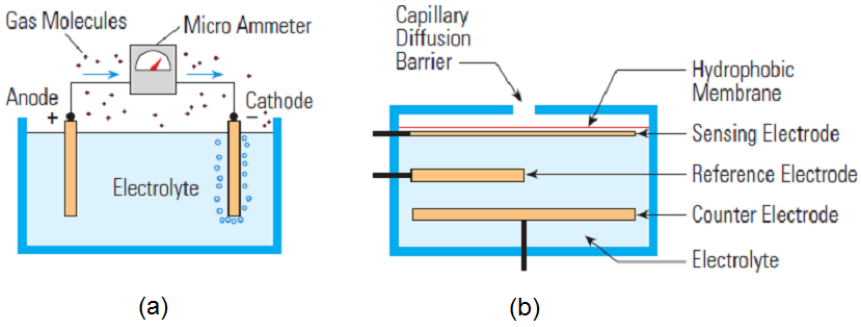

Figure 2.8. Schematic representations of typical electrochemical gas sensors with (a) two-electrode design, and (b) three-electrode design.

2.2.5. Catalytic Gas Sensors

Pellet resistor sensors called pellistors which are sometimes referred to as catalytic bead sensors, have widely been used for the indirect detection of combustible gases for more than 50 years. Pellistor detectors consist of two coils of fine platinum wire both embedded in a ceramic mass, (e.g., a bead of alumina) and connected electrically in a Wheatstone-bridge circuit. One of the ceramic beads is impregnated with a special catalyst which promotes oxidation, whilst the other without catalysts inhibits oxidation.

Current is passed through the coils so that they reach a temperature at which oxidation of the combustible gas readily occurs at the catalyzed bead of the active pellistor (T > 450 °C) in the presence of oxygen in an exothermic reaction.

$$CH_4 + 2O_2 + (N_2 + O_2) \rightarrow CO_2 + 2H_2O + (N_2 + O_2) + \text{heat} \qquad (2.3)$$

During operation, the flammable vapor or gas comes into contact with each of the pellistors. The generated heat of the heterogeneous catalysis causes an increase of the resistance of the conductive wire. The inactive bead (or compensator) is present to minimize the environmental effects such as temperature, heat conductivity variation of the ambient atmosphere and humidity. As both elements behave similarly with temperature and humidity variations, no imbalance is seen in the bridge circuit, when no combustive gas is present. The change in resistance, however, causes an imbalance in the Wheatstone-bridge circuit which is proportional to the concentration of combustible gas present.

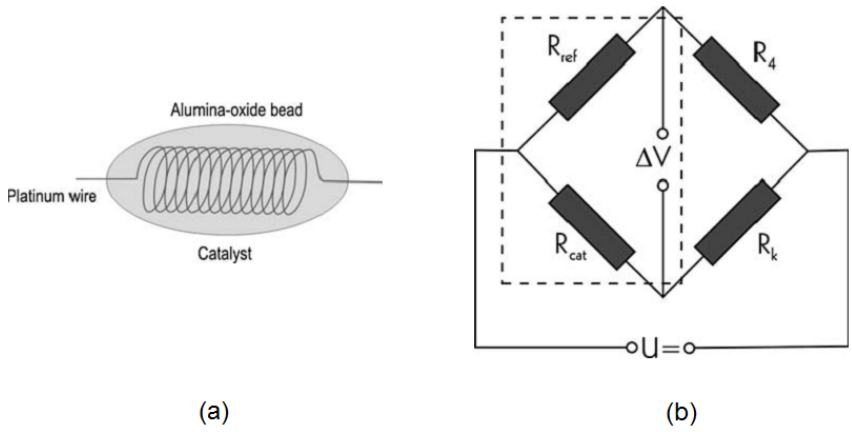

Figure 2.9. Structure of a conventional pellistor (a) and Wheatstone-bridge configuration of pellistors (b). (Source: Barsony et al., 2009)

2.2.6. Acoustic Wave Gas Sensors

Acoustic wave devices are based on high-frequency mechanical vibrations. They provide a simple, direct and sensitive method for probing the chemical and physical properties of materials. The utilization of acoustic wave devices for gas-phase sensing applications relies on their sensitivity towards small changes (perturbations) occurring at the “active” surface. In order to monitor a specific gas or vapor, a sensitive layer is generally employed. In the presence of an analyte species, the waves’ properties become perturbed in a measurable way that can be correlated to the analyte concentration (Ballantine et al., 1989).

Virtually all acoustic-wave-based devices use a piezoelectric material to generate the acoustic wave which propagates along the surface or throughout the bulk of the structure. Piezoelectricity is the ability of certain crystals to couple mechanical strain to electrical polarization. By applying a time-varying electrical field, a synchronous mechanical deformation of the piezoelectric material will arise, resulting in the coincident generation of an acoustic wave in the material, and vice versa (Ballantine et al., 1989; Wohltjen et al., 1979).

Acoustic wave devices come in a number of configurations, each with their own distinct acoustic and electrical characteristics. Two different groups of acoustic wave devices that are commonly employed for gas sensing can be classified. The first are bulk acoustic wave (BAW) devices, which concern acoustic wave propagation through the bulk of the structure. This category of devices includes the quartz crystal microbalance (QCM) and thin-film resonators (TFRs), the latter encapsulating thin-film bulk acoustic resonator (TFBAR) and solidly mounted resonator (SMR) structures. The second type utilize acoustic waves confined to the surface of the piezoelectric material, and are known as surface acoustic wave (SAW) devices. Schematic diagrams of these can be seen in Figure 2.10 (Ippolito et al., 2009).

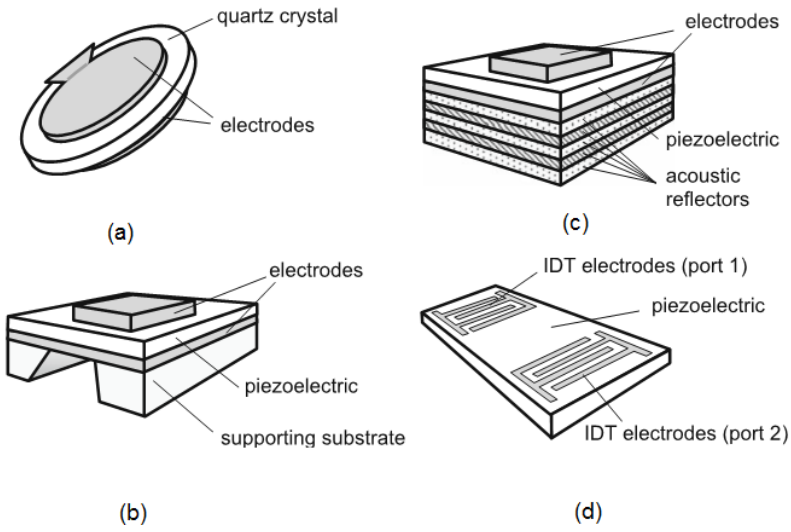

Figure 2.10. Schematic diagrams of (a) QCM, (b) TFBAR, (c) SMR, and (d) SAW.

CHAPTER 3

THEORY, METHOD AND MATERIALS

3.1. Adsorption Phenomena

3.1.1. The Surface of Solids

The inherent property of confining a definite space is perhaps the most distinguishing property of a solid. The boundary, which is characteristic of a solid, is called “surface”.

On a crystallographic level, every solid can be identified by its atomic or molecular arrangement. This arrangement, which is specific to each solid, constitutes a solid phase.

Generally, the identification of such a structure (atomic positions, cohesive energy) is defined in the scope of an infinite crystal, which implies a similar environment for all atoms. But, near the surface this is no longer true and it is important to consider a new local structure of atoms or electrically charged species.

In the particular case of ionic species, to achieve local electro-neutrality, it will often be necessary to take the solid’s environment into account. The material and the different phases in contact with it will thus reach equilibrium.

This forms the concept of an interface: a privileged area of the solid, from which all interactions are likely to start and develop between solid and different surrounding compounds upon contact.

Depending on the nature of these compounds, there will be cases of solid-solid, solid-liquid or gas-solid reactions.

To conceptualize the solid-gas reactions, it is essential to start by simply picturing a molecule of gas bonding with a solid. The bonded molecule could remain independent from its support or react with it (Figure 3.1).

In the first case, the reversible process responsible is adsorption, which then constitutes the overall reaction. It is called the adsorption-desorption phenomenon.

In the second case, adsorption will be the first step of a more complex process. It has, in this case, a non-reversible character due to which a new compound, GS for instance, will form.

The nature of the observed phenomenon will depend on the thermodynamic conditions (pressure, temperature) as well as on the chemical affinity of the existing species.

Adsorption phenomena can be distinguished between physical and chemical adsorption. Chemical adsorption or chemisorption is characterized by a simple electron transfer between the gas in physisorbed state and the solid. This transfer results in a reversible chemical bond between the two compounds (Figure 3.1b). Once again, the appearance of the chemisorption process is directly related to the environment's thermodynamic conditions.

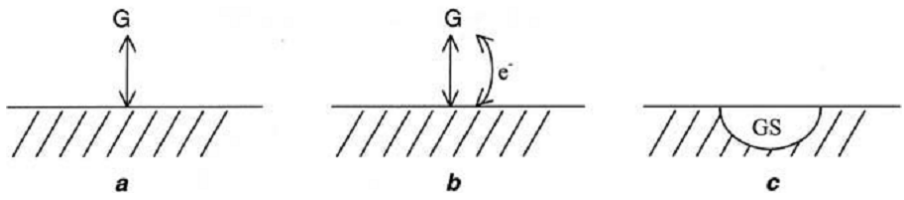

Figure 3.1. The different interaction modes between a gas and a solid. (a) physical adsorption – physisorption, (b) chemical adsorption – chemisorption, and (c) non-reversible reaction.

3.1.2. van der Waals Forces

By analogy with molecular interactions, we can use the forces known as van der Waals forces to interpret the source of the physical adsorption processes which are favored by low temperatures. These forces, denoted by $\vec{F}$ for instance, are associated with a scalar potential φ:

$$\vec{F} = -\vec{grad}\,\varphi$$

The scalar potentials are additive and the global scalar potential is the sum of the potential of attraction φ_a and the potential of repulsion φ_r:

$$\varphi = \varphi_a + \varphi_r$$

where,

$$\varphi_a = -\frac{C}{r^6} \quad \text{and} \quad \varphi_r = -\frac{B}{r^n}$$

r represents the intermolecular distance, while the constant C consists of three contributions:

- the Keesom interaction or Keesom force, which only applies to polar molecules and originates from the attraction between several molecules' permanent dipoles,
- the induction interaction or Debye force, which originates from a molecule's polarizability. It is caused by the attraction between permanent dipoles and other dipoles that are induced by the permanent dipoles,
- London's dispersion force, which originates from the attraction between molecules' instantaneous dipoles. This is generally the most powerful attraction.

As for the expression of φ_r, this is an empirical expression for which we generally choose n=12.

The global scalar potential φ between two molecules is thus given by,

$$\varphi = \frac{B}{r^{12}} - \frac{C}{r^6} \tag{3.1}$$

If we take into account the fact that the potential reaches a minimum, φ_0, at equilibrium, meaning for an intermolecular distance r_0, we then obtain,

$$\varphi = \varphi_0 \left[2\left(\frac{r_0}{r}\right)^6 - \left(\frac{r_0}{r}\right)^{12} \right] \tag{3.2}$$

3.1.3. Chemical Forces between a Gas Species and the Surface of a Solid

If a gas atom has free electrons, a chemical bond between the gas and the solid becomes plausible, and there are two extreme polarization possibilities that can be observed, either:

$$G + e^- \Leftrightarrow G^-$$

or,

$$G \Leftrightarrow G^+ + e^-$$

This physicochemical aspect is crucial in explaining the fundamental working principles of chemical sensors.

3.1.4. Distinction between Physical and Chemical Adsorption

The difference between physical and chemical adsorption is due to the difference between the natures of forces that keep the gas molecules on the solid's surface.

Analysis of the $\Phi = f(r)$ curve reveals that it goes through a minimum defined by Φ_0 and r_0.

In physical absorption (Figure 3.2 (a)), the value of Φ_0 is so much smaller than that observed for chemical adsorption. r_0, on the contrary, is lower for chemical adsorption.

Consequently, physical adsorption can be considered as a non-activated and therefore "spontaneous" process that is likely to take place at relatively low temperatures.

On the other hand, chemisorption is an "activated" process and the $\Phi = f(r)$ curve first goes through a maximum marked by the activation energy value E_A.

The necessity of activation is related to the fact that electron transfer, from the gas or solid, requires an energy input, implying the existence of a kinetic process.

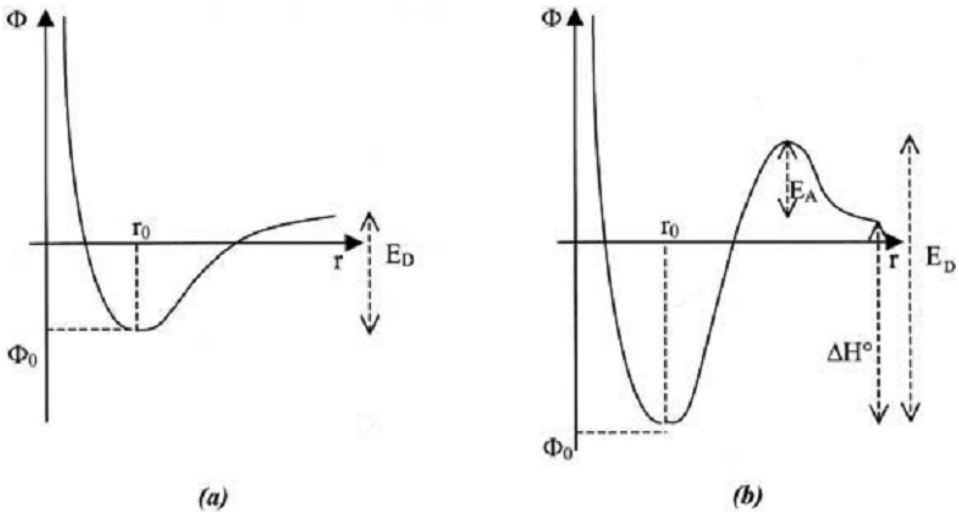

Figure 3.2. Plots of $\Phi = f(r)$ in case of (a) physisorption, (b) chemisorption.

3.1.5. Physical Adsorption Isotherms

There are two extremities to be considered concerning the mobility of the layers that become adsorbed on the surface of a solid:

i. molecules that are adsorbed in the form of mobile layers
ii. molecules that are perfectly located on some of the solid "surface" sites

The existence of these extremities can be explained by the non-uniformity of the solid's surface potential and its relation to the periodicity of a crystal lattice and the nature of the solid's constituents.

This periodicity (Figure 3.3) can be described by assuming there are sites of lower energy E_1, separated by higher energy E_2 levels.

The probability of a molecule translating from one stable site to another is thus dependent on $E_2 - E_1$. The $E_2 - E_1$ difference represents the energy barrier needed to be overcome to initiate this species' surface movement.

If $kT >> E_2 - E_1$, the probability of a transition is high, and this renders the layer as mobile.

If $kT << E_2 - E_1$, the probability of a transition is low, and this renders the layer as localized.

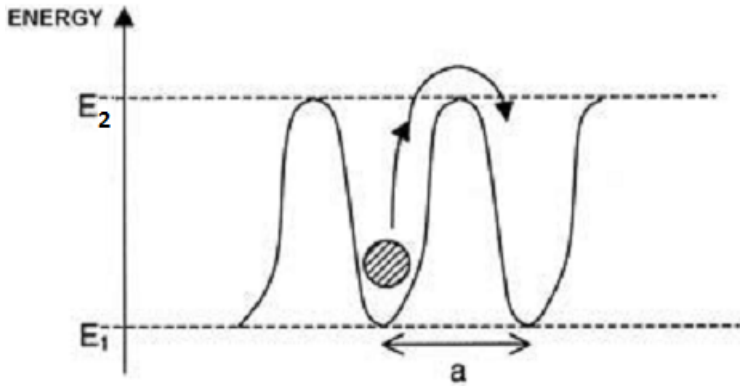

Figure 3.3. Periodic change in the surface energy of a crystal with lattice parameter a.

Beyond this classification, it is also relevant to consider the case of monolayer adsorption as well as multilayer adsorption.

3.1.5.1. Adsorption Isotherms of Localized Monolayers

The adsorbed molecule is bound in a low energy position; this position constitutes an active site.

The solid's surface is made up of identical active sites that we will be assimilated by active species, which is denoted by s.

Adsorption can then be expressed as an actual chemical reaction for which the following notations will be used:

- [A] represents a compound A in gaseous state,
- << A >> is for a constituent A in a solid or liquid solution,
- < A > is for a pure solid or liquid phase of compound A.

In this case, the adsorption reaction is expressed by:

$$[G] + << s >> \Leftrightarrow << G - s >>$$

Here, << G – s >> is the new species formed, and therefore a G – s will exist in solution s.

To express the equation of the isotherm, there are two complementary and equally effective methods present.

3.1.5.2. Thermodynamic Model

If the mass action law is applied to the previous equilibrium,

$$K = \frac{\left|<< G - s >>\right|}{P\left|<< s >>\right|} \tag{3.3}$$

where K is the equilibrium constant. It is expressed by,

$$K = K_0 \exp\left(-\frac{\Delta H^\circ}{RT}\right) \tag{3.4}$$

Adsorption is an exothermic process, which leads to $\Delta H^\circ < 0$. A negative value for ΔH° means that the reverse reaction takes place if the temperature increases. Therefore, adsorption is more likely to take place at low temperatures.

In an ideal solution, if S denotes the number of free sites, S_0 denotes the number of sites, and θ represents the fraction of sites that are in use, which is expressed as,

$$\theta = \frac{S_0 - S}{S_0} = \left|<< G - s >>\right| \tag{3.5}$$

then,

$$\left|<< s >>\right| = \frac{S}{S_0} = 1 - \theta \tag{3.6}$$

which yields,

$$K = \frac{\theta}{(1-\theta)P} \tag{3.7}$$

and therefore,

$$\theta = \frac{KP}{1+KP} \tag{3.8}$$

This relation, which is called the Langmuir isotherm, demonstrates that the percentage coverage of the surface is a homographic function of pressure. This function is an accurate way to represent most adsorption-related experimental results.

Note that, at low surface coverage fractions ($\theta << 1$), a proportionality law similar to Henry's law is obtained:

$$\theta = KP \tag{3.9}$$

3.1.5.3. The Kinetic Model

An equilibrium is reached if the variable resulting from two dynamic processes is brought to zero:

- adsorption, which has a rate R_F;
- desorption; which has a rate R_D;

These two processes can be seen as two elementary steps that do not involve any intermediate reactions.

In such a case, the R_F rate is proportional to the number of shocks υ, which is the number of molecule and surface impacts per unit time, as well as to the number of free sites on the surface.

$$R_F = \alpha\upsilon(1-\theta) \tag{3.10}$$

where,

$$\upsilon = P \Big/ \sqrt{2\pi\, m\, kT} \tag{3.11}$$

therefore,

$$R_F = \alpha' P(1-\theta) \tag{3.12}$$

R_D is proportional to the number of already adsorbed molecules, so,

$$R_D = \beta\theta \tag{3.13}$$

At equilibrium, $V_F = V_D$, which leads to,

$$\theta = \frac{KP}{1+KP} \tag{3.14}$$

where,

$$K = \alpha' / \beta \tag{3.15}$$

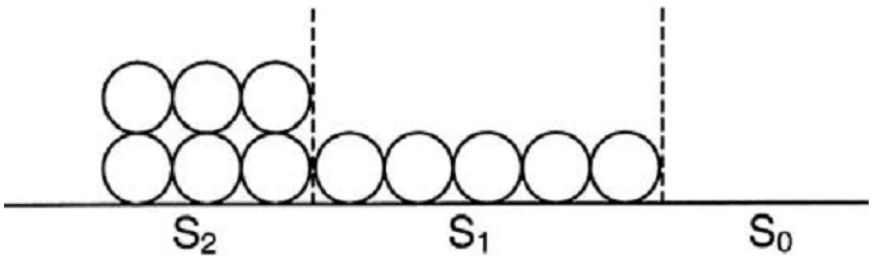

Figure 3.4. Parceling of the solid's surface depending on the number of layers.

3.1.6. Chemical Adsorption

Figure 3.5 shows the Lennard-Jones representation of gas adsorption over a surface when adsorption is accompanied by decomposition of the molecule into separate atoms. Adsorption proceeds from physisorption (a) – weak adsorption associated with van der Waals forces, such as dipole interactions – to chemisorption (b) – strong bonding, charge transfer between adsorbent and adsorbate, since less energy E_a is required than the total energy E_{dis} to dissociate the molecule. Therefore, physisorption is the first step of association of gas species with a solid surface, afterwards the physisorbed species can be chemisorbed if they exchange electrons with the solid surface.

Physisorption is a slightly exothermic process ($\Delta H_{phys}<0$) characterized by high surface coverage θ at low temperatures and a low surface coverage at high temperatures. If the partial pressure is very low, Henry's law applies and the amount of physisorbed species is simply proportional to the partial pressure.

Desorption, like chemisorption, requires some energy $E_d = Q_{chem} + E_a$. So, in contrast to physisorption, that is slightly exothermic, inactivated process, chemisorption and desorption are activated processes. The activation energies can be supplied either thermally or by a non-equilibrium process.

The net rate of chemisorption is given by:

$$\frac{d\theta}{dt} = k_{ads} \exp\left(-\frac{E_a}{kT}\right) - k_{des}\theta \exp\left(-\frac{E_a + \Delta H_{chem}}{kT}\right) \tag{3.16}$$

where, θ is the fraction of chemisorbed available surface sites, k_{ads} and k_{des} are the rate constants for adsorption and desorption.

At steady state the equilibrium coverage results:

$$\vartheta = \frac{k_{ads}}{k_{des}} \exp\left(\frac{\Delta H_{chem}}{kT}\right) \tag{3.17}$$

and θ decreases rapidly with increasing temperature.

Experimentally the heat of adsorption ΔH_{chem} decreases with coverage θ, mainly because of the heterogeneity of the surface – high energy sites will be occupied first and low-energy ones later. On the contrary, activation energy E_a can be regarded as the difference in the electrochemical potential between the semiconductor surface and the adsorbed oxygen and therefore increases with increasing coverage θ, due to the reduction of available surface electrons n_s.

When an adsorbate acts as a surface state capturing an electron or a hole, chemisorption is often called "ionosorption".

An important ubiquitous species that ionosorbs over MOX surfaces is water. The chemisorption of water onto oxide from air can be very strong, forming a "hydroxylated surface", where the OH^- ion is bounded to the cation and the H^+ ion to the oxide anion. The overall effect of water vapor is to increase surface conductance.

The study of oxygen ionosorption is of particular importance for MOX gas sensors which are operated in an atmospheric environment.

In the temperature range between 400 and 800 K oxygen ionosorbs over MOX in a molecular (O_2^-) and atomic form (O^-):

$$\begin{aligned} O_{2,gas} &\Leftrightarrow O_{2,ads} \\ e^- + O_{2,ads} &\Leftrightarrow O_{2,ads}^- \\ e^- + \frac{1}{2}O_{2,ads}^- &\Leftrightarrow O_{ads}^- \end{aligned} \tag{3.18}$$

Since O_2^- has a lower activation energy it dominates at temperatures up to 500 K, at higher temperatures O^- form dominates.

In many cases the gas detection process is intimately related to the reactions between the species to be detected and ionosorbed surface oxygen. When a reducing gas such as CO comes into contact with the MOX surface, the following reactions that consume ionosorbed oxygen add to Equation 3.3:

$$\begin{aligned} CO_{gas} &\rightarrow CO_{ads} \\ CO_{ads} + O_{ads}^- &\rightarrow CO_{2,gas} + e^- \end{aligned} \tag{3.19}$$

The overall effect is a decrease of the equilibrium density of ionosorbed oxygen that is detected as an increase in sensor conductance.

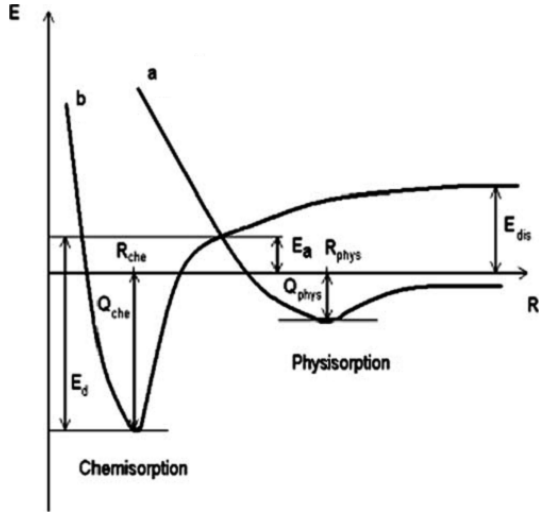

Figure 3.5. Lennard-Jones model for (a) physisorption and (b) chemisorption.

3.2. The Piezoelectric Effect and Principles of QCM

Piezoelectricity, first described by the Curie brothers in 1880 and further elaborated by Gabriel Lippmann in 1881, is the ability of certain crystals to elastically deform by the application of a voltage and vice-versa. This allows transduction between electrical and acoustic energy.

Applying a periodic perturbation (electric field/voltage) to a piezoelectric material results in an elastic deformation (strain) that travels through the solid as a wave. These waves propagate in an elastic medium either as longitudinal (compression) or transverse (shear) lattice deformations, or as a combination of both. The propagation of the wave is often described or categorized in terms of the material lattice points' oscillatory pattern, which are termed as 'wave modes' (Ballantine et al., 1996).

Figure 3.6 depicts the associated lattice point deformations for the three simplest cases, namely longitudinal, transverse and Rayleigh modes. It should be noted that the lattice point deformation of the Rayleigh mode is just a combination of both the longitudinal and transverse modes.

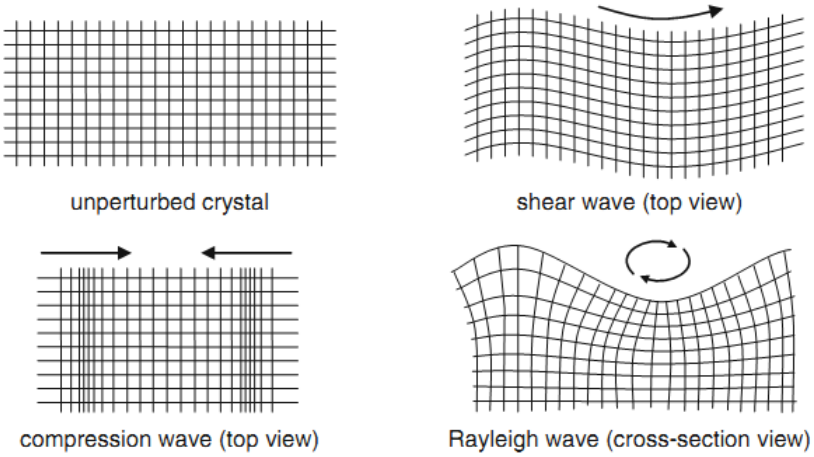

Figure 3.6. Some propagation modes for acoustic wave devices.
(Source: Ippolito et al., 2009)

Quartz is a form of silicon dioxide (SiO_2) that has triclinic crystal symmetry, and is by far the most commonly utilized piezoelectric material for sensing applications. Like all piezoelectric materials, it is anisotropic, i.e. its material properties vary with different crystallographic orientations and there are no planes of material symmetry. Therefore, an acoustic wave device can exhibit different resonance frequencies and vibration modes depending on the chosen crystallographic orientation. Hence, the

acoustic mode, phase velocity, propagation direction, temperature coefficient etc. of the device are predominantly determined by the selected piezoelectric material's crystallographic orientation. For instance, deviation in the crystal plane of quartz by as little as 0°5′ can be advantageously used to engineer the temperature coefficient of the structure (Auld, 1990).

Figure 3.7 shows two commonly employed crystal cuts of quartz. In the case of AT-cut quartz, the crystal is cut at 35°15′ angle with respect to the optical axis (z-axis), where the temperature coefficient of the crystal is at its smallest value.

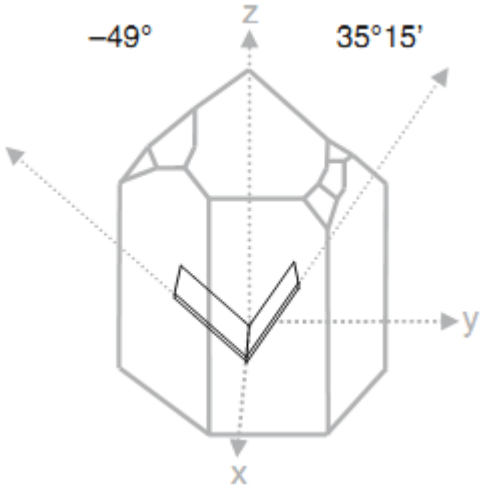

Figure 3.7. Quartz crystal showing the AT-cut (35°15′) and BT-cut (-49°) which belong to the Y-cut family.

The most commonly used acoustic-wave-based sensors are quartz crystal microbalances (QCMs). They have an extensive history of use for the quantification of physical and chemical adsorption in both commercial and fundamental research applications. Initially the devices were developed by Walter Cady in 1921 for stabilizing electronic oscillators, in which case they were labeled quartz crystal resonators (QCR). However, when employed for sensing, they are most commonly referred to as quartz crystal microbalances or QCMs, since the response is predominantly due to the mass loading of the analyte on the electrode surface. Although a large number of crystals exhibit piezoelectricity, quartz possesses a unique combination of mechanical, electrical, chemical and thermal properties. These properties have led to its commercial significance.

QCMs attained importance as analytical devices following the discovery of their linear relationship between mass loading and the frequency response, as described in 1959 by Sauerbrey (Sauerbrey, 1959). A QCM typically consists of a thin circular AT-cut quartz crystal, which support thickness shear modes. Both sides of the device are patterned with metallic pads that form the electrodes. Although it is possible for the electrode to be comprised of any metallic material, for gas-sensing experiments a noble metal such as gold is generally utilized as it does not readily oxidize in air. The electrodes are used to excite acoustic bulk waves. The addition of gas-sensitive layer on top of one or both of the electrode pads, as seen in Figure 3.8, is used to make the device sensitive to a target gas or vapor species (King, 1964).

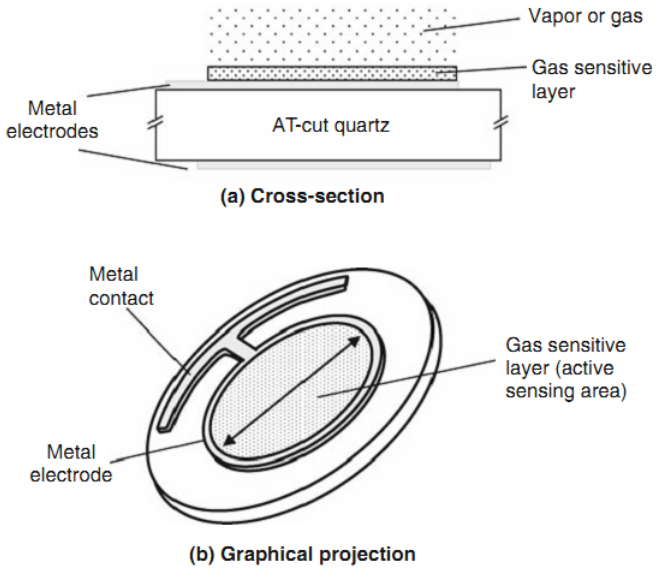

Figure 3.8. (a) Cross section and (b) graphical projection of a QCM, illustrating a gas sensitive layer on one electrode.

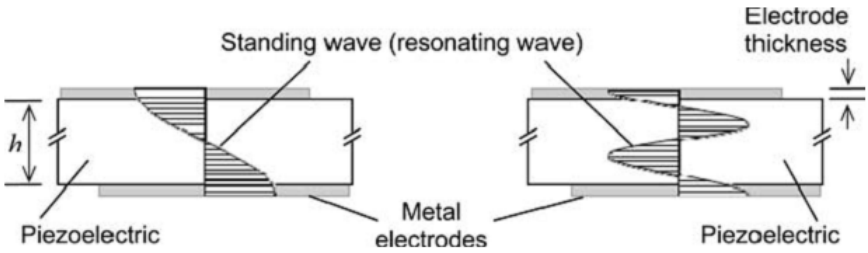

Figure 3.9. Cross-section view of a thickness-shear-mode resonator showing the standing wave of the fundamental and 3rd harmonic.

QCMs gained prominence in the 1960s and 70s for monitoring the thickness of layers during their deposition in vacuum, and are still routinely used as in-situ thickness monitors (Buck et al., 2004). They are well suited to such applications as they are capable of measuring small mass changes equivalent to a layer several nanometers thick. Subsequently, they have been modified to operate as gas-phase sensors by adsorption of target gas molecules onto the active sensing area (Cheeke et al, 1999). They are commercially available at operating frequencies up to 100 MHz, however for gas-sensing applications generally 5-30 MHz structures are used because higher frequency devices require thinner quartz layers, which are extremely fragile.

3.2.1. Mass Deposition Calculations

Assuming a quartz crystal electrode of thickness *t* and weigh *m*, the wavelength λ of the standing wave at resonance frequency is:

$$\lambda = \frac{2t}{n} \tag{3.20}$$

where *n* is the harmonic number. This equation holds true as long as the QCM electrode is made up of a piezoelectric material and an oscillating electric field applied across the device induces an acoustic wave propagating through the bulk of the crystal that meets the minimum impedance (corresponding resonance frequency) condition *when the thickness of the device is an integer multiple of the half wavelength of the acoustic wave* (Ebersole et al., 1990). In addition, for *n*=1, the frequency is *F* and for higher harmonics *n* should be more than 1. The acoustic shear wave velocity ν is defined as:

$$\nu = \lambda F \tag{3.21}$$

therefore, the frequency for the first harmonic will be:

$$F = \frac{\nu}{2t} \tag{3.22}$$

The shift in frequency resulting from an infinitesimal change in thickness can be evaluated by differentiating both sides of the equation with respect to *t*:

$$dF = -\frac{\nu}{2t^2}dt \tag{3.23}$$

Dividing Equation (3.23) by (3.22) yields the "frequency stability",

$$\frac{dF}{F} = -\frac{dt}{t} \tag{3.24}$$

Equation (3.24) can be expressed in terms of the mass of coated film per unit area M and change in mass per unit area ΔM,

$$\frac{\Delta F}{F} = -\frac{\Delta M}{M} \tag{3.25}$$

In this derivation, the net change in mass ΔM is assumed to be homogenously distributed over the surface of the crystal. Therefore, the change in mass ΔM per unit area is proportional to total mass change $\Delta M_{crystal}$ on the entire surface of the crystal. This means acoustic shear wave velocity is the same across the entire crystal surface. If M and ΔM in Equation (3.25) are expressed in terms of the thickness t_f of the thin-film material deposited on unit area of the crystal and density ρ_f of it, then the frequency stability or relative frequency change will be,

$$\frac{\Delta F}{F} = -\frac{\rho_f t_f}{\rho t} \tag{3.26}$$

Substituting resonance frequency F in Equation (3.22) in (3.26) yields,

$$\frac{\Delta F}{F} = -\frac{\rho_f t_f 2F}{\rho \nu} \tag{3.27}$$

Pulling t_f from Equation (3.27) and rearranging gives,

$$t_f = -\frac{\Delta F}{2F^2}\frac{\rho \nu}{\rho_f} \tag{3.28}$$

Here, F, ρ and v are material properties inherent to the crystal and production process (i.e. density, crystal cut). According to this relation, QCM can be utilized as a thickness monitor in case the density of the coated material is known. From Equation (3.27), a crystal constant can be defined as,

$$C_q = \frac{2}{\rho v} \tag{3.29}$$

So, the relationship between frequency shift and mass change can be rewritten as,

$$\Delta F = -C_q F^2 \Delta M_f \tag{3.30}$$

The change in resonance frequency can be expressed as,

$$\frac{\Delta F}{F} = -C_q F \Delta M_f \tag{3.31}$$

This relation is known as Sauerbrey equation (Sauerbrey, 1959). Different derivations and forms of this equation is available, however, in essence, the change in mass by material deposition on the crystal can simply be obtained by the aid of measured resonance frequency shift. Consequently, the shift in frequency is directly related with the mass change.

An alternative form of Sauerbrey equation relating mass change in terms of frequency shift, comprising intrinsic material properties of the crystal can be written as,

$$\Delta f = -\frac{2 f_0^2}{A\sqrt{\rho\mu}} \Delta m \tag{3.32}$$

Here; f_0, A, μ and ρ are, operating frequency of the QCM crystal, active area of gold coated electrode surface area on the crystal, shear modulus and density of the quartz crystal, respectively.

It should be noted that the Sauerbrey equation assumes a uniform distribution of mass over the active sensing area of the device, as the shear amplitude decreases from the center to the electrode edges (Ward et al., 1990).

Using the Rayleigh hypothesis, which assumes that the added mass layer does not affect the peak kinetic and potential energies (Ballantine et al., 1996), the mass sensitivity S_m of a QCM for per unit area A of added mass can be defined as (Wenzel et al., 1989).

$$S_m = \lim_{\Delta m \to 0} \frac{\Delta f / f_0}{\Delta m / A} \tag{3.33}$$

where, $f_0 \approx \upsilon_0 / 2h_0$, with υ_0 and h_0 being the acoustic velocity and the thickness of the unloaded resonator respectively, and $m_0 = \rho A h_0$ is the initial mass of the resonator.

This only hold true for total added mass amounts that is less than 2% of the resonator's initial mass.

The QCM electrodes used throughout this study were made from AT-cut quartz crystals operating at a fundamental resonance frequency of 7.995 MHz and works within an operating frequency range of 7.995 MHz to 7.950 MHz. The crystals have a density of 2.684 g/cm^3, shear modulus of 2.947×10^{11} g/cm.s^2 and gold coated electrode surface area of 0.196 cm^2. Plugging these data into Equation (3.32) yields,

$$\Delta f = -1.15 \times 10^{-5} f_0^2 \Delta m \tag{3.34}$$

This translates into a mass change of 1.34 ng due to a net shift of 1 Hz in the oscillation frequency of a crystal initially operating at a base frequency of 7.995 MHz.

3.2.1.1. Non-linear QCM Response

Under some circumstances, non-linear effects such as diffusion of water molecules into or from an adsorbing film coating may necessitate modification of well established models to properly explain the humidity adsorption and desorption kinetics.

Consider a polymer film coating for humidity sensing applications. As the humidity concentration in the surrounding atmosphere increases, adsorbed water molecules are associated with more other water molecules, increasing the water content on the surface, which is based on grams of sorbed water per one gram of dry coating material.

It is reasonable to think that one water molecule can be adsorbed on the monomer unit by dipole–dipole interactions and the excess water molecules are adsorbed on the readily sorbed water molecule with hydrogen bonding (cluster formation) in the amorphous region of the polymer film.

In the sorption process of water, first the water molecules diffuse in the polymer film and are fixed at a critical point by dipole-dipole interactions between the water molecule and the polymer. Second, the sorbed water associates with the neighboring waters and forms the cluster. The sorption processes may be expressed as follows:

$$H_2O \text{ (atmosphere)} \leftrightarrow H_2O \text{ (in film) (diffusion)}$$
$$H_2O \text{ (in film)} + \text{film} \leftrightarrow H_2O_{ad} \text{ film (dipole – dipole)}$$
$$H_2O_{ad} \text{ film} + nH_2O \leftrightarrow (n+1)\, H_2O_{ad} \text{ film (hydrogen bonding)}$$

The difference in the oscillation frequency shift (Δf) of a QCM is directly proportional to change in the mass of QCM due to adsorption and desorption. A fundamental relationship between surface adsorption kinetics and frequency shift of a QCM can be expressed as;

$$\frac{d\Delta f}{dt} = -\left(K_a C + K_d\right)\Delta f + K_a C \Delta f_{\max} \tag{3.35}$$

where, Δf, t, K_a, K_d, and C are oscillation frequency shift of QCM, time, adsorption and desorption rate constants, and concentration of sorbed species, respectively.

The Langmuir model, which was developed by Irving Langmuir in 1916 to analyze the sorption kinetics of gas molecules onto solid surfaces, describes the rate of surface reactions for forming a monolayer on a solid surface using the relation below (Langmuir, 1916);

$$\frac{d\theta}{dt} = k_a\left(1-\theta\right)C - k_d\theta \tag{3.36}$$

Here, θ is surface coverage fraction which is a unitless quantity, k_a and k_d are rate constants for the adsorption and desorption processes, and C is concentration.

Equations (3.35) and (3.36) can be used interchangeably, since oscillation frequency shift of QCM Δf is directly proportional to the adsorbed mass which is a function of surface coverage fraction θ.

Returning to the example, in the region where the number of the sorbed water per monomer unit of polymer is less than unity, sorbed water is linearly proportional to the surface coverage θ, thus the frequency shift of the QCM according to Langmuir adsorption isotherm model which is employed to explain the relationship between the surface adsorption kinetics and frequency shift Δf of QCM. However, the formation of a cluster, which is essentially the agglomeration of nanotubes and nanoparticles by the necks formed by the adsorbed water molecules, leads to a viscoelastic phase that cannot keep up with the resonance frequency of the quartz crystal. This causes an energy dissipation yielding the non-linear QCM response. So, in order to properly explain the experimental results according to the predictions of Langmuir model, some modifications have to be made considering this effect (Baleanu et al., 2011).

3.3. Materials

3.3.1. Carbon Nanotubes

During experiments to elucidate the growth mechanism of buckyballs (C_{60}) using an arc-discharge method, Iijima discovered elongated hollow structures in carbon soot which were multi-wall CNTs (Iijima, 1991).

These elongated hollow structures are a crystalline form of carbon which has significantly different properties compared to other forms of carbon, which are graphite and diamond. They exhibit peculiar mechanical, electronic and optical properties superior to other materials and have been a focus of intensive research since their discovery.

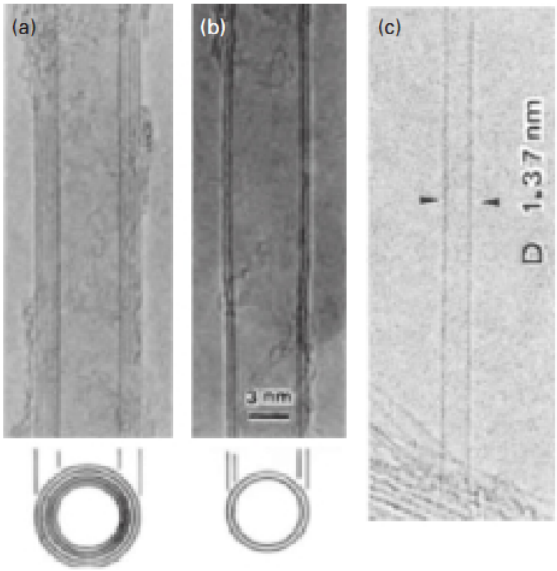

Figure 3.10. High resolution TEM images of (a) multi-wall, (b) double-wall, and (c) single-wall CNTs observed by Sumio Iijima. (Source: Iijima, 1991)

A single-wall carbon nanotube (SWCNT) can be visualized as a graphene sheet rolled up into a hollow cylinder of a one-dimensional tubular wire with a diameter that ranges from about 0.5 nm to 5 nm and lengths on the order of micrometers to centimeters. A multi-wall carbon nanotube (MWCNT) is similar in structure to a single wall CNT but has multiple nested or concentric cylindrical walls with the spacing between walls comparable to the interlayer spacing in graphite, approximately 0.34 nm. The ends of a CNT are often capped with a hemisphere of the buckyball structure (Reich et al., 2004).

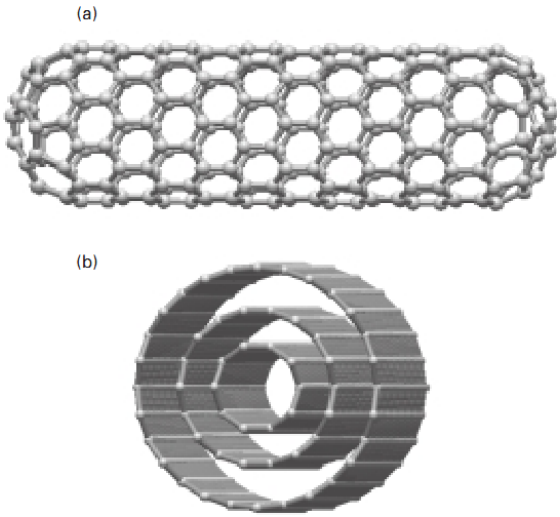

Figure 3.11. Illustration of (a) an ideal single-wall CNT with hemispherical caps at both ends, and (b) a multi-wall CNT.

Being the building block of carbon nanotubes, carbon is a Group IV element which is capable of producing various different molecular compounds and crystalline solids. It has four valance electrons, which interact with each other to produce many different carbon allotropes. Elemental carbon's four valance electrons occupy the 2*s* and 2*p* orbitals, as shown in Figure 3.12. When carbon atoms approach each other to form a crystal, one of the 2*s* electrons is excited to the empty $2p_z$ orbital harnessing the energy gained from the neighboring nuclei, which favors lowering the total energy of the system. Therefore, interactions or bonding involve the 2*s* and 2*p* orbitals of neighboring carbon atoms. This mixing of atomic orbitals is explained by the hybridization theory in chemistry. Hybridization is the formation of new orbitals formed by mixing of atomic orbitals called as "hybrid orbitals" (Figure 3.12 (b)). The existence of multiple types of hybridization in carbon yields different allotropes of carbon.

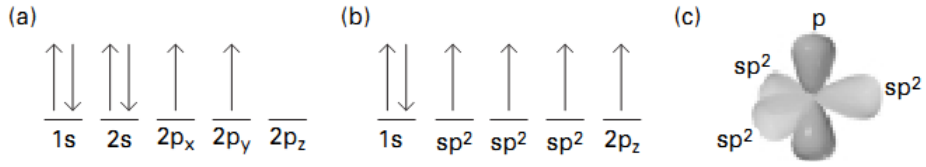

Figure 3.12. The filling of electrons in atomic orbitals and their relative spins in (a) elemental carbon, (b) graphene. 2s and two of the 2p orbitals interact to form three sp^2 hybrid orbitals, which lie on the same plane with 120° angles between each other. (c) Depiction of the three hybrid sp^2 orbitals and one unhybridized p_z orbital positioned perpendicular to the hybridized sp^2 orbitals.

Graphene is a planar allotrope of carbon where carbon atoms are covalently bonded on a one-atom thick single plane. Figure 3.13 shows the experimental observation of the planar honeycomb structure of graphene (Reich et al., 2004).

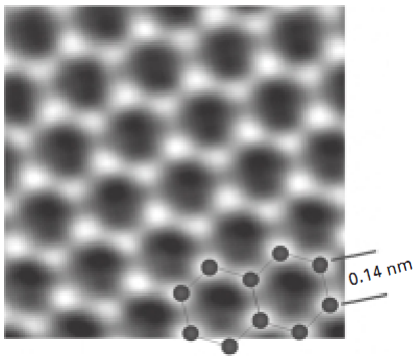

Figure 3.13. Transmission aberration-corrected microscope (TEAM) image of graphene, clearly showing the carbon atoms and bonds in the honeycomb structure. (Source: Berkeley's TEAM05, 2009)

Graphene is the starting point of three carbon allotropes. Wrapping graphene into a sphere produces buckyballs, folding into a cylinder produces nanotubes, and stacking several sheets of graphene forms graphite (Figure 3.14) (Geim et al., 2007).

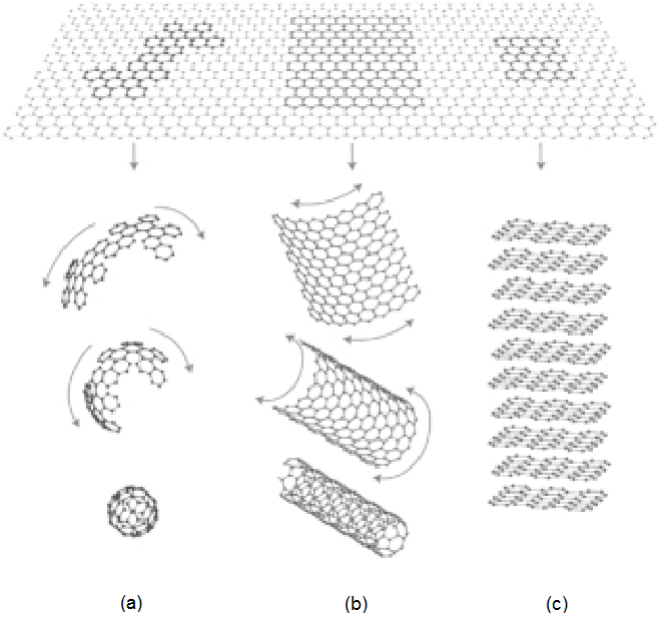

Figure 3.14. A two-dimensional graphene sheet can form, (a) zero-dimensional buckyball, (b) one-dimensional nanotubes, and (c) three-dimensional graphite.

In graphene, carbon atoms are bonded by the interaction of the three sp^2 hybrid orbitals making three bonds with neighboring carbon atoms called σ bonds. They are the strongest type of covalent bonds, with electrons localized along the plane connecting carbon atoms and are responsible for the exceptional strength and mechanical properties of graphene and carbon nanotubes. The $2p_z$ electrons, where the electron cloud is

distributed perpendicular to the plane connecting carbon atoms, are loosely bound to the nuclei and are relatively delocalized. They either form covalent bonds called π bonds or participate in interactions between two different planes of carbon atoms via a mechanism called "π-π stacking". These delocalized electrons are responsible for the electronic properties of graphene and carbon nanotubes.

Table 3.1. Allotropes of graphene and their properties.
(Source: Saito et al., 1995)

Dimension	**0D**	**1D**	**2D**	**3D**
Allotrope	C_{60} buckyball	Carbon nanotubes	Graphene	Graphite
Structure	Spherical	Cylindrical	Planar	Stacked planar
Hybridization	sp^2	sp^2	sp^2	sp^2
Electronic properties	Semiconductor	Metal or semiconductor	Semi-metal	Metal

The key concept used to identify and describe the different configurations of CNTs and their resulting electronic band structure is "chirality", which is a term derived from the Greek word "*kheir*" meaning "hand". Chirality or "handedness" is used to describe the reflection symmetry between an object and its mirror image. Formally, *a chiral object is an object that is not superimposable on its mirror image*; and conversely, *an achiral object is an object that is superimposable on its mirror image*.

Understanding the concept of chirality is essential, because it is used to classify the physical and electronic structure of CNTs. The CNTs that are superimposable on their own mirror images are classified as *achiral CNTs*, and all other nanotubes that are not superimposable are classified as *chiral CNTs*. To be clearer, all single-wall CNTs are either chiral or achiral. Moreover, achiral CNTs are further classified as armchair CNTs or zigzag CNTs, depending on the geometry of the nanotube circular cross-section. To summarize briefly, there are three types of single-wall CNT: chiral CNTs, armchair CNTs, and zigzag CNTs, of which the latter two are achiral and their symmetry often makes them easier to explore and gain broad insight. The three types of single-wall CNT and their associated geometrical cross-sections are shown in Figure 3.15.

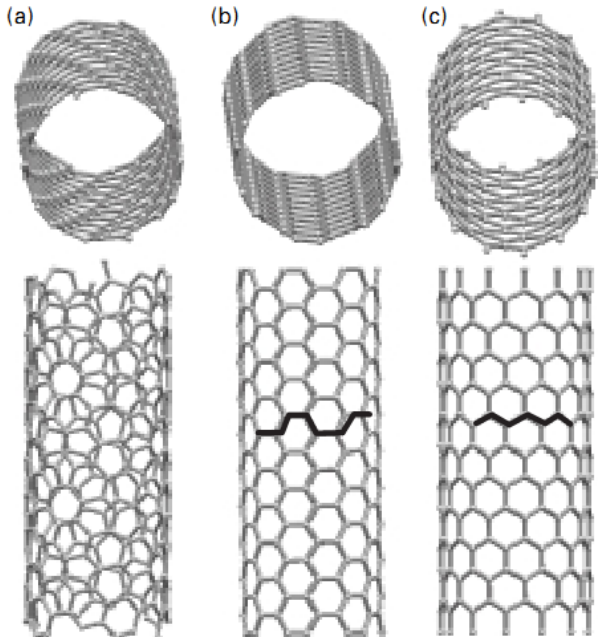

Figure 3.15. The three types of single-wall CNT: (a) A chiral CNT, (b) an armchair CNT, and (c) a zigzag CNT. The cross-sections of the latter two illustrations have been highlighted by the bold lines showing the armchair and zigzag character respectively.

3.3.2. Iron Oxide Nanoparticles

Along with a lack of consensus on the exact definition of what a nanoparticle is, on the basis that the unique optical, magnetic, and chemical properties owing to their miniscule sizes essentially start to vanish as their sizes approach to 40-50 nm range, it is practical to define nanoparticles as particles whose sizes in at least two dimensions are smaller than 40 nm (Huber, 2005).

Nanoparticles of iron oxide, in particular, magnetite (Fe_3O_4) and its oxidized form maghemite (γ-Fe_2O_3) were used as functional materials for gas sensing applications in this thesis study.

Magnetite has an inverse spinel structure in which oxygen anions form a face-centered cubic crystal system. In magnetite structure, all tetrahedral lattice sites are occupied by Fe^{3+} cations, whereas octahedral lattice sites are occupied by both Fe^{3+} and Fe^{2+} cations.

Maghemite structure is different from magnetite in the aspects that all or most of the Fe atoms are in trivalent state (Fe^{3+}) and by the presence of cation vacancies in the octahedral sites. Maghemite has a cubic unit cell which contains 32 O ions, 21⅓ Fe^{3+}

cations and 2⅔ vacancies. The cations are distributed randomly over the 8 tetrahedral and 16 octahedral sites.

Iron has 4 unpaired electrons in its 3*d* shell, so it has a strong magnetic moment due the uncancelled spin magnetic moments of the unpaired electrons. Fe^{2+} cations also have 4 unpaired electrons in their 3*d* shells and Fe^{3+} cations have 5 unpaired electrons in their 3d shell. Therefore, in crystals formed containing iron atoms or Fe^{2+} and Fe^{3+} ions they can be in ferromagnetic, antiferromagnetic or ferrimagnetic states.

Iron oxide nanoparticles, typically in the size range of 5-15 nm are superparamagnetic, which is a novel property encountered only in these dimensions due to the peculiar behavior of magnetic properties at the nanoscale. They have been intensively explored not only for their scientific but also many practical and technological applications: such as, high-density magnetic storage media, biosensing applications, medical applications like targeted drug delivery, hyperthermia therapy, contrast agents in magnetic resonance imaging (MRI), and magnetic inks for ink-jet printing (Laurent et al., 2008; Philippova et al., 2011).

3.3.3. Ferrocene

Organo-transition metal chemistry has its origins to the serendipitous discovery of an organo-iron compound, ferrocene. Ferrocene is an iron complex with the formula $Fe(C_5H_5)_2$. It was unintentionally obtained by Kealy and Pauson in 1951 while they were trying to couple cyclopentadienyl radicals to isolate dicyclopentadienyl. They attempted to oxidize cyclopentadienylmagnesium bromide by ferric chloride because it was a common practice to treat a Grignard reagent with ferric chloride to form a hydrocarbon. However, it is assumed that the Grignard reagent reduced the ferric chloride to ferrous chloride and they instead isolated ferrocene by the following reaction:

$$2C_5H_5MgBr + FeCl_2 \rightarrow C_5H_5FeC_5H_5 + MgBr_2 + MgCl_2 \qquad (3.37)$$

Chemists Wilkinson, Rosenblum, Whiting, and Woodward also deserve credit for their separate discoveries that ferrocene must be a sandwich compound. Indeed, ferrocene is a type of organometallic chemical compound called “metallocene” with two cyclopentadienyl (Cp) rings bound on opposite sides of a central iron atom. The iron

atom located between the two Cp rings generally has +2 oxidation state. Each Cp ring is allocated a single negative charge, raising the number of π-electrons on each ring to six, hence making them aromatic. Six electrons from each Cp ring are shared with the iron atom via covalent bonding. Coupled with the six *d*-electrons on Fe^{2+}, the complex attains a stable 18-electron inert gas configuration (Jolly, 1970; Williamson, 2004; Stepnicka, 2008). This property renders it resistant to water, acids and oxidation.

Ferrocene (Fc) is utilized as the modifier material to functionalize carbon nanotubes and iron oxide nanoparticles in this thesis study.

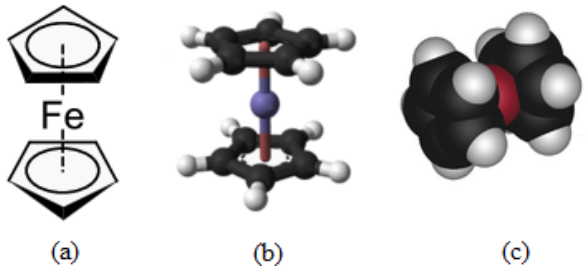

Figure 3.16. Structural representations of ferrocene: (a) full skeletal formula, (b) ball-and-stick model, (c) space-fill model.

3.4. Gases

In the table below, chemical and electronic structures, along with calculated dipole moment values for gases used in this study are given as a reference. These data will be used to explain the characteristics and mechanisms of interactions between the sensitive coating materials and the gas molecules.

Table 3.2. Chemical and electronic structures of gas molecules used in this study.

Gas	Chemical Structure	3D Structure and Dipole Moment
Carbon dioxide	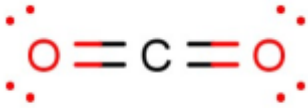	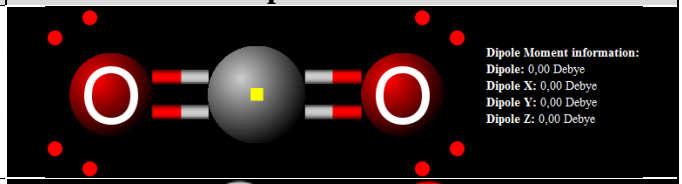
Carbon monoxide	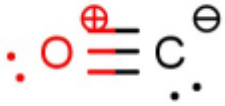	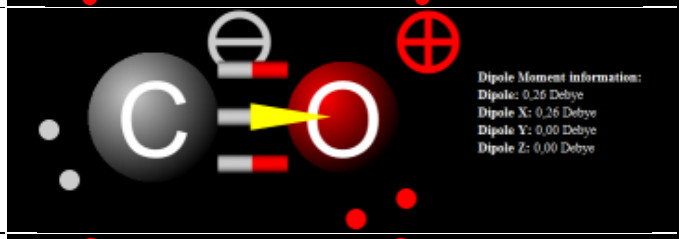
Oxygen	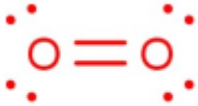	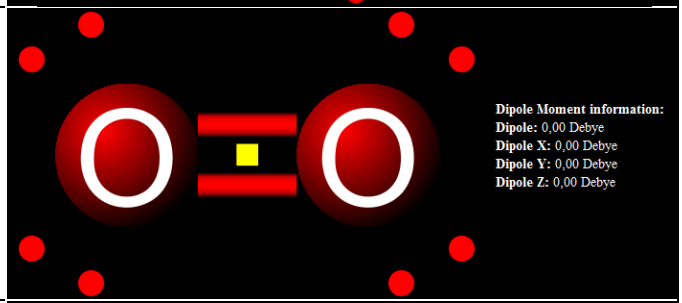
Water vapor	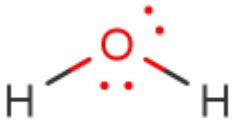	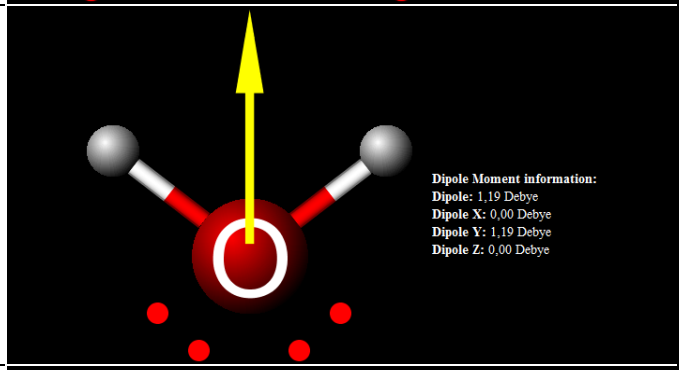
Nitrogen		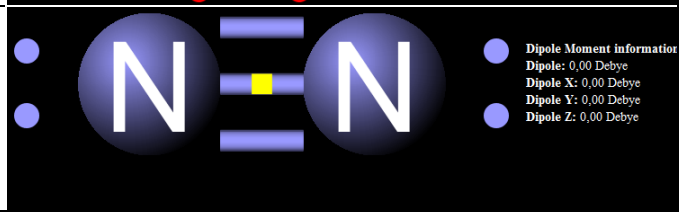

CHAPTER 4

EXPERIMENTAL

In this study, gas sensing properties of ferrocene (Fc) modified and unmodified multi-wall carbon nanotubes (MWCNT) and iron oxide nanoparticles were investigated via acoustic wave and electrical based techniques.

In the succeeding sections; preparation of the dispersions of each nanoparticle, coating of thin-films onto quartz crystal microbalance (QCM) and gold interdigitated (IDE) electrodes, and the gas flow control and signal acquisition system utilized in the course of gas sensitivity assessments are explained in detail.

From this point on, the samples will be mentioned with code names assigned to them with respect to their material bases. The nomenclature is presented in Table 4.1.

Table 4.1. Codenames assigned to the samples with respect to their material bases.

Multi-wall carbon nanotube	**MWCNT**
Ferrocene modified multi-wall carbon nanotube	**MWCNT-Fc**
Iron oxide nanoparticles	**FeO**
Ferrocene modified iron oxide nanoparticles	**FeO-Fc**

4.1. Material and Sample Preparation

In this thesis, commercially obtained amine ($-NH_2$) functionalized multi-wall carbon nanotubes (O.D. < 20 nm, I.D. ~ 4 nm, L ~ 1-12 μm, purity > 99 wt%, Cheap Tubes Inc., Vermont, USA) were used as the base materials for Fc modified CNTs.

Iron oxide nanoparticles were synthesized by the alkaline coprecipitation of ferric and ferrous salts according to the following reaction:

$$FeCl_2 \cdot 4H_2O + 2FeCl_3 \cdot 6H_2O + 8NH_4OH \rightarrow Fe_3O_4 + 8NH_4Cl + 20H_2O$$

Since magnetite (Fe_3O_4) is highly susceptible to oxidation, some of it was transformed to maghemite (γ-Fe_2O_3) in the presence of atmospheric oxygen.

MWCNTs and iron oxide nanoparticles were modified with Fc according to the procedures depicted in Figure 4.1 and Figure 4.2, respectively.

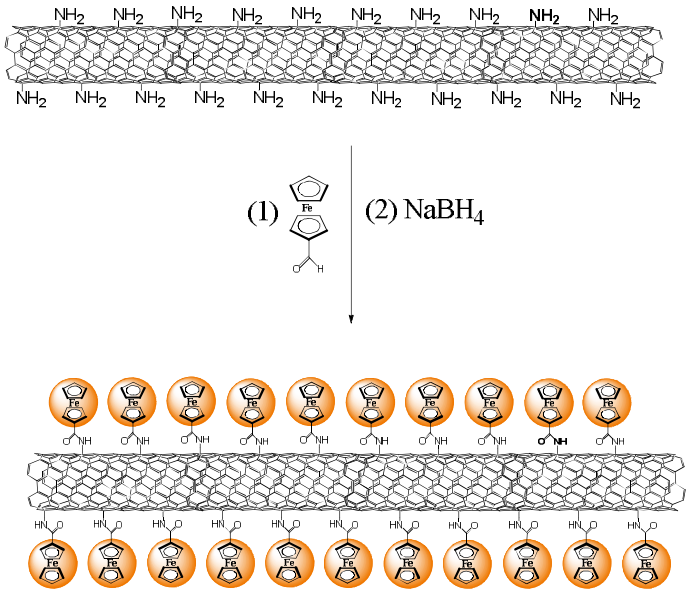

Figure 4.1. Modification scheme for amine ($–NH_2$) functionalized MWCNTs with Fc molecules.

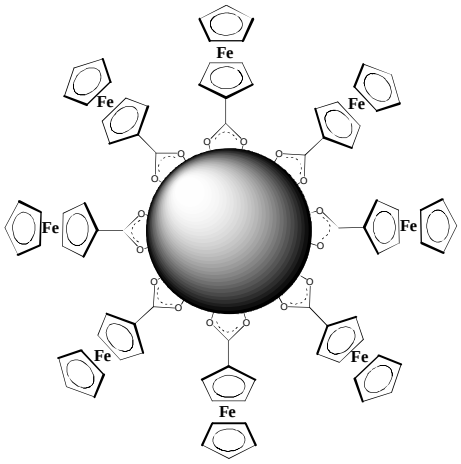

Figure 4.2. Modification scheme for iron oxide nanoparticles with Fc molecules.

Minute amounts (on the tip of a micro-spoon spatula) from each one of the ferrocene modified along with the unmodified MWCNTs and iron oxide nanoparticles were mixed with 3 mL ethanol inside glass vials to obtain homogenous liquid dispersions suitable for thin-film coating procedure.

All the prepared dispersions were sonicated for 12 h in order to ensure adequate homogeneity.

The QCM electrodes were thoroughly cleaned with acetone, ethanol, isopropyl alcohol and distilled water, respectively in an ultrasonic bath prior to the coating process.

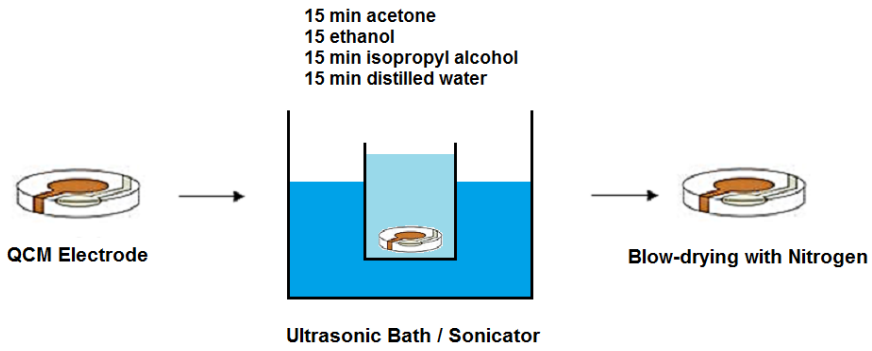

Figure 4.3. QCM electrode cleaning procedure.

5 μL from each of these dispersions were drawn from the vials via a micro pipette and then drop-cast onto AT-cut gold coated quartz crystal microbalance (QCM) and gold interdigitated (IDE) glass electrodes. The coated electrodes were dried on hotplate at 60 °C for 30 min to deposit thin-films.

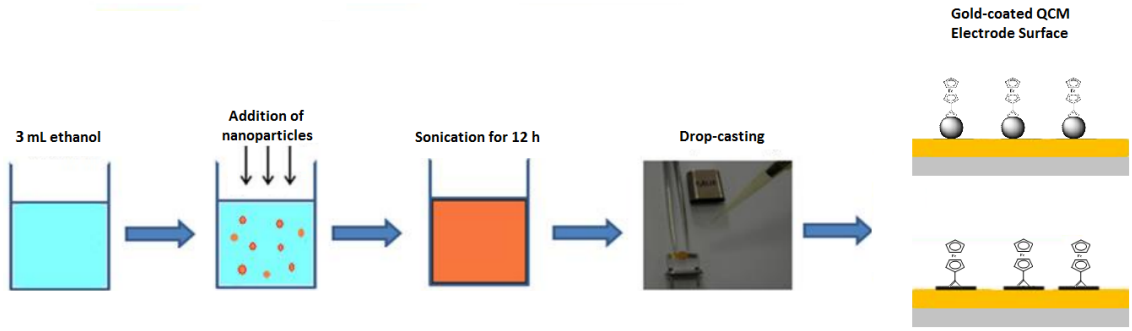

Figure 4.4. Preparation of nanoparticle dispersions and deposition of thin-films onto QCM electrodes by drop-casting technique.

As previously stated, according to Sauerbrey relation, a net shift of 1 Hz in the oscillation frequency of a crystal initially operating at a base frequency f_0 of 7.995 MHz translates into a mass change of 1.34 ng due to homogenous mass variations on the crystal surface with a gold coated electrode surface area of 0.196 cm^2.

This fact is exploited to determine the mass of the deposited thin-film material on the QCM electrode by calculating the frequency difference Δf_0 after thin-film deposition and evaluating that value into mass according to Sauerbrey equation.

Figure 4.5. Cleaned (left) and thin-film coated QCM crystals (right).

4.2. Gas Flow Control and Signal Measurement System

The gas flow control and measurement system is composed of three main parts:

The first part is comprised of N_2 (99,99 pure), O_2 (99,99 pure), CO_2 (99,99 pure) and CO (10.000 ppm N_2 blend) gas tubes and 6 MKS 179A Mass-Flo mass-flow meters (MKS Instruments, Massachusetts, USA) rated with 1x20 sccm (calibrated with CO), 2x100 sccm (calibrated with CO and N_2), 2x1000 sccm (calibrated with CO and N_2), 1x2000 sccm (calibrated with N_2) flow ranges, linked to an 8-channel MKS Type 647C multichannel gas flow controller unit (MKS Instruments, Massachusetts, USA). The multichannel gas flow controller unit is connected to a PC via RS-232 interface and operated remotely using a purpose-built LabVIEW program.

Figure 4.6. Overview of the experimental setup showing all components together.

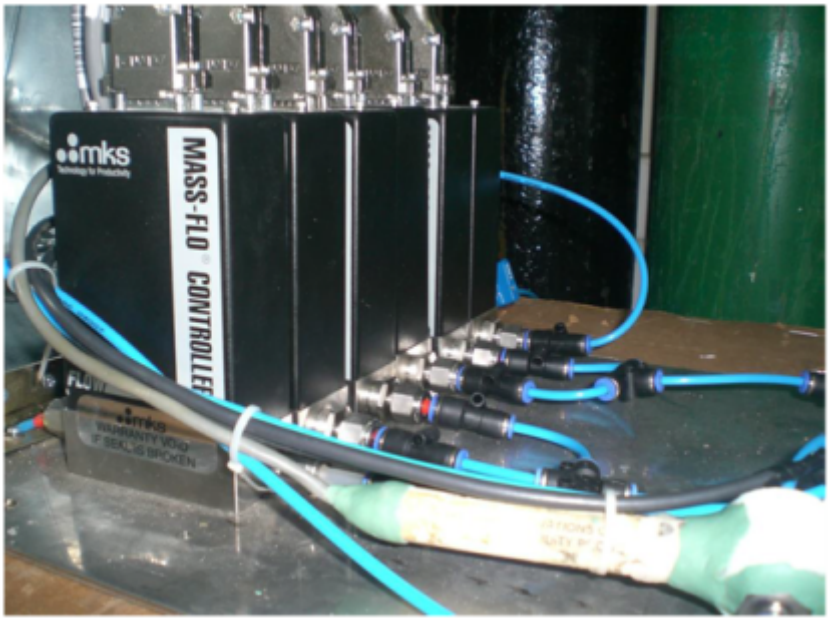

Figure 4.7. Array of 6 MKS 179A Mass-Flo mass-flow meters used for regulating gas flow into the measurement cell.

Figure 4.8. 8-channel MKS Type 647C multichannel gas flow controller unit.

Gas measurement cell constitutes the second part of the system. Essentially, it is a hermetically sealed glass vial having gas inlet/outlet pipes and electrical contact pads for QCM and IDE electrodes with terminals leading outside the cell. The cell is placed in a metallic enclosure along with the mass-flow meters, which is practically a Faraday cage, to avoid electromagnetic interference from external sources. This both protects the sensitive equipment against harmful EMI and provides signal integrity.

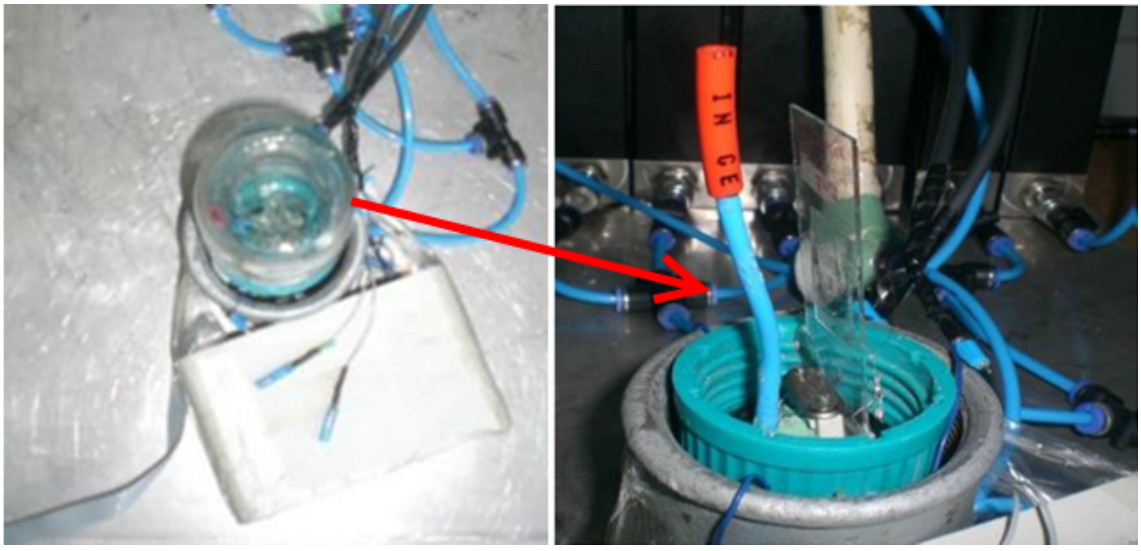

Figure 4.9. Gas measurement cell and oscillator circuit (left). Close-up view of the gas measurement cell with the vial lid open, clearly showing the gas inlet pipe, electrical contact pads for QCM and IDE electrodes and a mounted IDE electrode (right).

Figure 4.10. Metallic enclosure where the gas measurement cell and mass-flow meters were placed. The enclosure functions as a Faraday cage to avoid electromagnetic interference from external sources. This both protects the sensitive equipment against harmful EMI and provides signal integrity.

Last part of the system contains a CHI 400B (CH Instruments, Austin, USA) time-resolved electrochemical quartz crystal microbalance (EQCM) analyzer with an oscillator circuit and a Keithley 2636A SYSTEM (Keithley Instruments, Ohio, USA) SourceMeter.

Figure 4.11. CHI 400B time-resolved electrochemical quartz crystal microbalance (EQCM) analyzer.

CHI 400B EQCM analyzer is connected to a PC via USB interface. Device control and data acquisition were performed via CHI Version 12.02 software bundled

with the device, whereas, Keithley 2636A SYSTEM SourceMeter's control and data acquisition were performed via RS232 and the same purpose-built LabVIEW program.

Figure 4.12. Keithley 2636A SYSTEM SourceMeter.

The QCM electrodes (International Crystal Manufacturing Co., Oklahoma, USA) used throughout this study were made from AT-cut quartz crystals with a fundamental resonance frequency of 7.995 MHz and works within an operating frequency range of 7.995 MHz to 7.950 MHz. The crystals have a density (ρ) of 2.684 g/cm^3, shear modulus (μ) of 2.947×10^{11} g/cm.s^2 and gold coated electrode surface area of 0.196 cm^2.

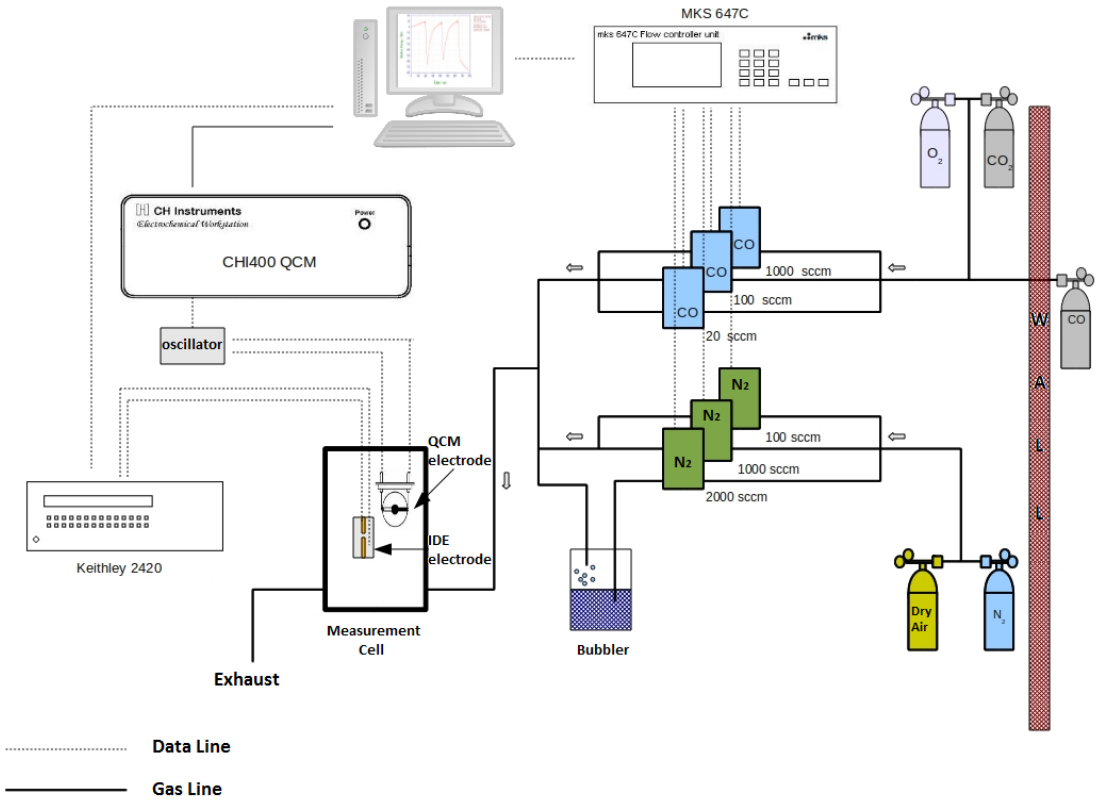

Figure 4.13. Detailed schematic overview of the gas flow and signal measurement system.

The thin-film coated electrodes were exposed to alternately varying levels of CO, CO_2, O_2 and humidity concentrations ranging from 0 vol% to 100 vol%. Concentrations of the inlet gases were adjusted by the mass flow meter array linked to the multichannel gas flow controller unit, which in turn, is computer controlled. Predetermined gas flow regimes (periodic, step and linear) with corresponding gas concentration levels were programmed via the purpose-built LabVIEW software. The test routines altered the concentration level of the inlet gas by mixing the active gas with desorption (inert) gas N_2 and maintained steady flow into the gas measurement cell during predetermined intervals.

In the periodic gas flow regime, active gas and desorption gas alternately switched on/switched off at full concentrations during 200 s intervals for two consecutive cycles to ensure consistency and to probe the repeatability of the experimental response (Figure 4.14).

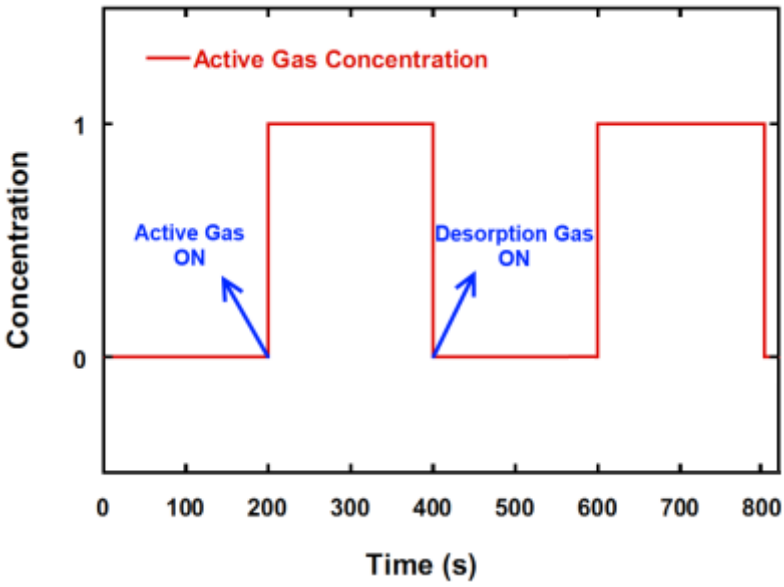

Figure 4.14. Concentration - time graph of periodic gas flow regime.

In the step gas flow regime, active gas concentration in the gas mixture raised with 20% increments from an initial value of 0% to 100%, whereas, desorption gas concentration in the gas mixture lowered with 20% decrements from an initial value of 100% to 0% during 200 s step intervals in the forward cycle. In the reverse cycle, active gas concentration in the gas mixture lowered with 20% decrements from 100% to 0%, whereas, desorption gas concentration in the gas mixture raised with 20% increments from 0% to 100% during 200 s step intervals (Figure 4.15).

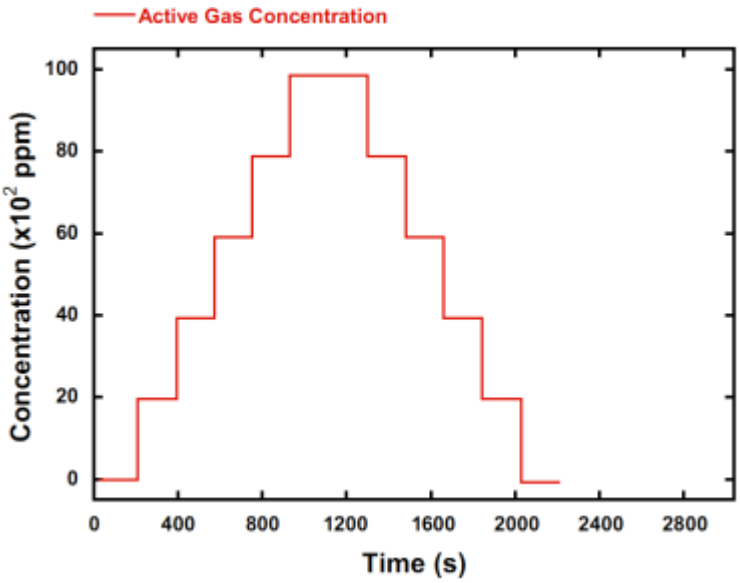

Figure 4.15. Concentration - time graph of step gas flow regime.

In the linear gas flow regime, active gas concentration in the gas mixture raised with 5% increments from an initial value of 0% to 100%, whereas, desorption gas concentration in the gas mixture lowered with 5% decrements from an initial value of 100% to 0% during 5 s step intervals in the forward cycle. In the reverse cycle, active gas concentration in the gas mixture lowered with 5% decrements from 100% to 0%, whereas, desorption gas concentration in the gas mixture raised with 5% increments from 0% to 100% during 10 s step intervals (Figure 4.16).

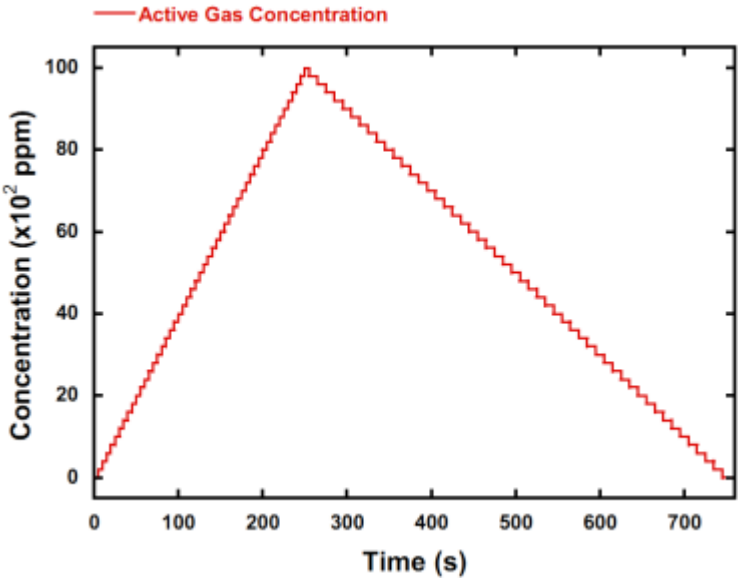

Figure 4.16. Concentration - time graph of linear gas flow regime.

A maximum gas flow rate of 500 sccm was attained for each one of the gas flow regimes during measurements.

Gas sensor responses of the thin-film coated QCM electrodes were determined by measuring the frequency shift (Δf) of the coated electrode due to gas sorption via the CHI 400B time-resolved (EQCM) analyzer.

Initial resonance frequency (f_0) values of each QCM electrode were recorded prior to coating. After coating, the resonance frequencies of each coated QCM electrode were recorded again. The frequency difference (Δf_0) after thin-film deposition was evaluated into the mass of the thin-film material (Δm_0) deposited on the QCM electrode according to Sauerbrey equation.

$$\Delta m_0 = 1.34\text{ng} \times \Delta f_0 \tag{4.1}$$

The mass of gas molecules (Δm) adsorbed on the surface of the thin-film coated electrode was calculated by plugging the frequency shift (Δf) value of the electrode due to gas sorption into Sauerbrey equation.

$$\Delta m = 1.34\text{ng} \times \Delta f \tag{4.2}$$

Finally, the sensitivity (S) of each sensor material to CO, CO_2, O_2 and humidity was defined as the ratio of the mass of gas molecules (Δm) adsorbed on the surface of the thin-film coated QCM electrode to the mass of the thin-film material (Δm_0) deposited on the QCM electrode per mil.

$$S = \frac{\Delta m}{\Delta m_0} \times 1000 \tag{4.3}$$

Substituting Δm and Δm_0 with Δf and Δf_0 respectively yields the frequency dependant form of the sensitivity relation,

$$S = \frac{\Delta f}{\Delta f_0} \times 1000 \tag{4.4}$$

On the other hand, responses from the interdigitated electrodes were assessed by measuring the resistance changes through the thin-film coating via the Keithley 2636A SYSTEM SourceMeter under a compliance current value of 1.0000 mA.

The sensitivity (S) of each sensor material to CO, CO_2, O_2 and humidity was defined as the ratio of the resistivity R_G of the thin-film coated IDE electrode under active gas/N_2 mixture atmosphere to the resistivity R_0 of the IDE electrode under pure N_2 atmosphere.

$$S = \frac{\left| R_g - R_0 \right|}{R_0} \tag{4.5}$$

CHAPTER 5

RESULTS AND DISCUSSION

In this part, surface morphologies and gas sensing properties of the nanoparticle thin-films were investigated by scanning electron microscopy (SEM), quartz crystal microbalance (QCM) and interdigitated electrode (IDE) techniques, respectively.

5.1. Surface Analysis of Deposited Nanoparticle Thin-Films

Surface morphologies of Fc modified and unmodified MWCNT/iron oxide nanoparticle thin-films deposited onto gold coated QCM electrodes by drop-casting technique were investigated by scanning electron microscopy (SEM).

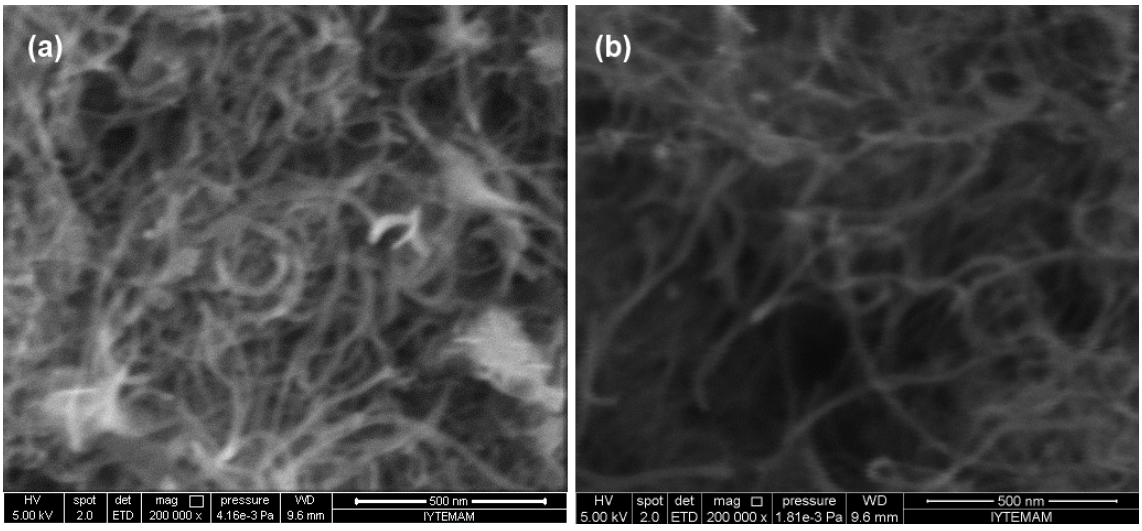

Figure 5.1. SEM images of (a) MWCNT and (b) MWCNT-Fc thin-films deposited on gold coated QCM electrodes.

In Figure 5.1 it is seen that both Fc modified and unmodified CNTs are homogenously distributed over the electrode surface. This indicates that long term sonication proved useful to mechanically unbundle CNTs enabling them to cover the electrode surface evenly. This is an important aspect since QCM method assumes a homogenous distribution of mass on the electrode surface to yield accurate and

repeatable results. Also gas interactions are much more efficient with functional materials dispersed on the electrode surface than the agglomerated case, since the dispersed state provides more interaction sites with the active gas molecules, thus increasing sensor response.

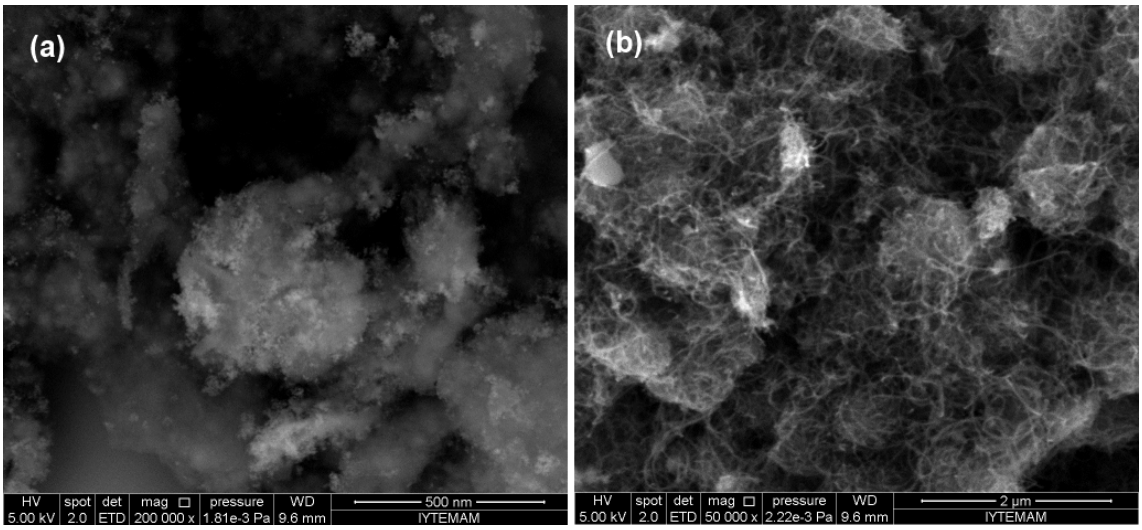

Figure 5.2. SEM images of (a) FeO and (b) FeO-Fc thin-films deposited on gold coated QCM electrodes.

Again, Figure 5.2 demonstrates homogenous formation of FeO and FeO-Fc nanoparticle thin-films, as the particles are spaced, dispersed and sized evenly. This is also a figure of merits for sensitive, selective and stable sensors.

5.2. Investigation of Gas Sensing Properties of Nanoparticles by QCM Technique

Gas adsorption and desorption characteristics that the nanoparticle thin-films exhibited towards CO, CO_2, O_2 and humidity were investigated by QCM technique and their sensitivity behaviors were assessed according to experimental data.

The initial assessments were carried out on a frequency shift response base. Further elaborations were made by sensitivity calculations according to the frequency shifts (Δf) after gas adsorptions and corresponding mass amount changes on the thin-film materials (Δm) deposited on the QCM electrodes (Equations 4.3-4.4).

In order to carry out sensitivity calculations, the shifts from initial resonance frequency (f_0) values of each QCM electrode prior to and after coating were recorded and the frequency differences (Δf_0) and (Δm_0) values were calculated according to Equation 4.1.

(Δf_0) and their corresponding (Δm_0) values that were used to convert frequency shift data into sensitivity data for each material are presented in Table 5.1.

Table 5.1. (Δf_0) and (Δm_0) values of the sample materials.

Sample	**Δf_0 (Hz)**	**Δm_0 (μg)**
MWCNT	6382	8.6
MWCNT-Fc	9874	13.2
FeO	17218	23.1
FeO-Fc	21608	29

5.2.1. Gas Measurement Results of Thin-Film Coatings

5.2.1.1. Gas Measurement Results of MWCNT/MWCNT-Fc Thin-Film Coatings

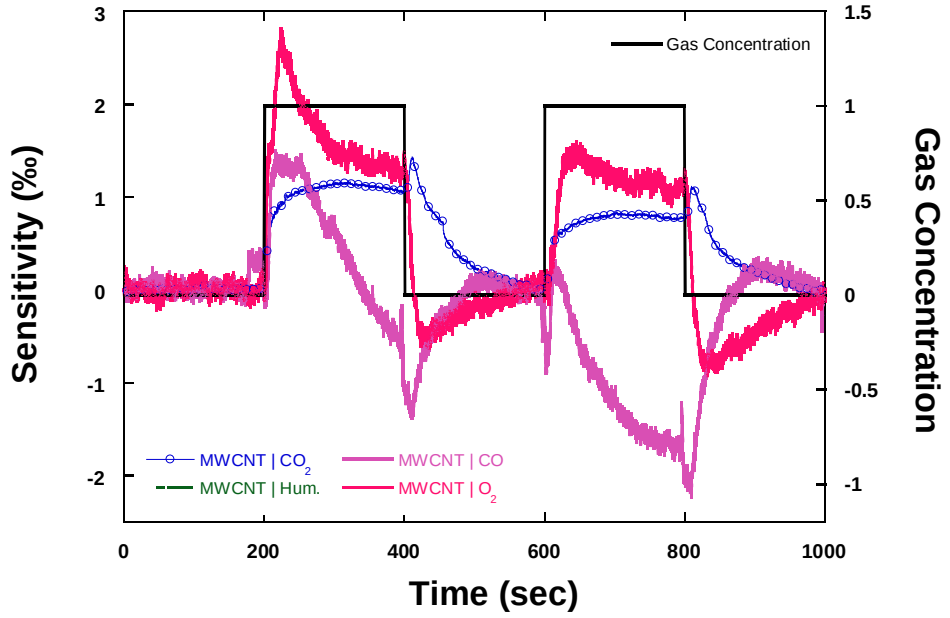

Figure 5.3. Gas responses of MWCNT thin-film coatings towards CO, CO_2, O_2 and humidity under periodic gas flow regime.

Figure 5.3 shows the sensitivity of MWCNT to CO, CO_2, O_2 and humidity under periodic gas flow regime. MWCNT exhibited a relatively low sensitivity towards the gases, on the order of a few per mil. Maximum sensitivity was observed towards O_2 gas. A partial non-linear QCM behavior was seen for CO in the second cycle of measurements. Humidity response of MWCNT could not be determined since no experimentally meaningful data could be acquired despite multiple attempts.

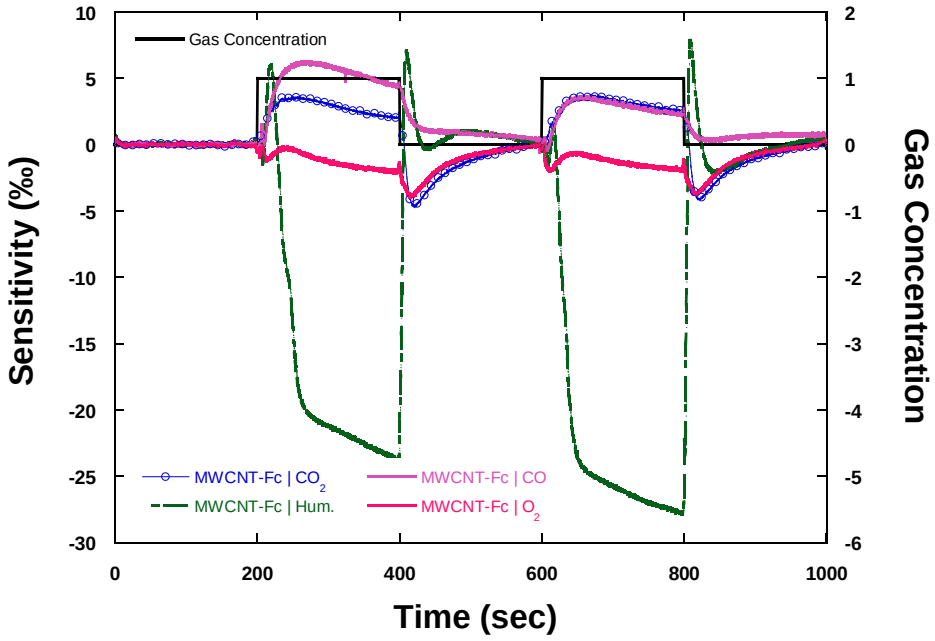

Figure 5.4. Gas responses of MWCNT-Fc thin-film coatings towards CO, CO_2, O_2 and humidity under periodic gas flow regime.

Figure 5.4 shows the sensitivity of MWCNT-Fc to CO, CO_2, O_2 and humidity under periodic gas flow regime. It is seen that ferrocene modification clearly improved the overall sensitivity of MWCNTs. This time, the maximum sensitivity was observed towards CO gas which can be attributed to the iron atom in ferrocene. Ferrocene induced humidity response of MWCNT, albeit, a strong non-linear QCM response was observed. This could be due to a formation of multilayer adsorbed water molecules at high humidity concentrations.

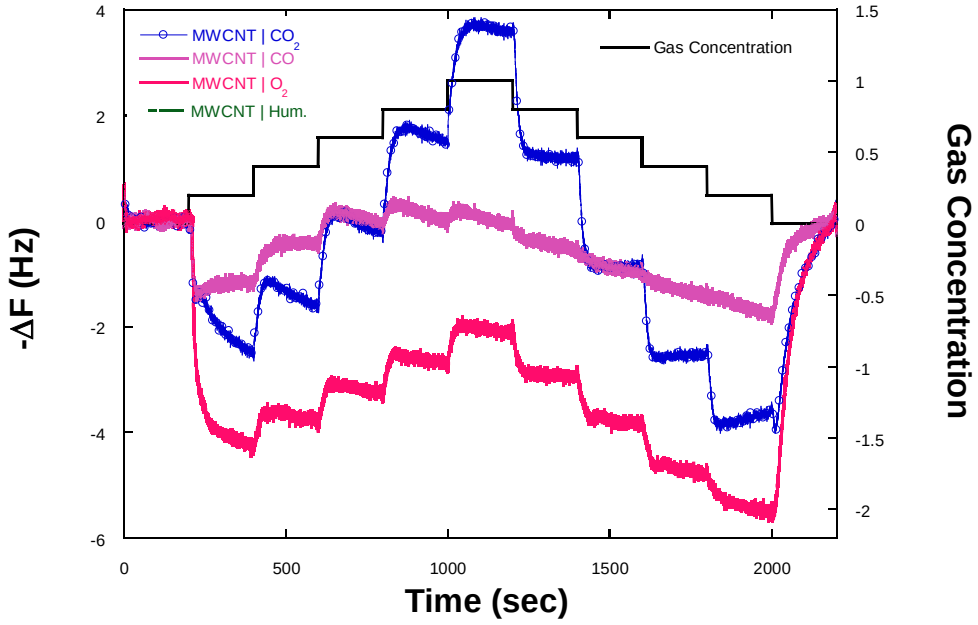

Figure 5.5. Gas responses of MWCNT thin-film coatings towards CO, CO_2, O_2 and humidity under step gas flow regime.

Figure 5.5 shows the frequency shift response of MWCNT to CO, CO_2, O_2 and humidity under step gas flow regime. A distinct non-linear QCM response was seen towards O_2 and CO. At the initial low concentrations, a rapid coverage of the film surface, accompanying with multilayer adsorption of O_2 and CO molecules was observed. However, by increasing gas concentrations, a gradual decrease in multilayer surface coverage that ultimately reached equilibrium at the maximum gas concentration was observed. This effect can be explained by the electrostatic repulsion of gas molecules to the multilayer adsorbed molecules on the surface. As the partial pressures of the gases increase in the gas mixture, O_2 and CO molecules impinging on the surface impose forces higher in magnitude than the forces binding multilayer adsorbed O_2 and CO molecules to the surface, thus removing multilayer adsorbed molecules from the surface, resulting in a gradual decrease from the initial non-linearity. This action clearly shows the prominent characteristics of a self-limiting reaction, since, as the O_2 and CO partial pressures decrease, multilayer adsorption is promoted again, restoring the initial non-linear effect.

Oxygen, normally a highly electronegative species with 8 unpaired electrons in its molecular form, is supposed to interact with the π-electrons of MWCNT inducing multilayer adsorption giving rise to the observed non-linear behavior. CO, on the other hand, already has a permanent dipole moment due to partial charges that can easily augment multilayer adsorption via strong electrostatic interactions with MWCNT. Humidity response of MWCNT could not be determined since no experimentally meaningful data could be acquired despite multiple attempts.

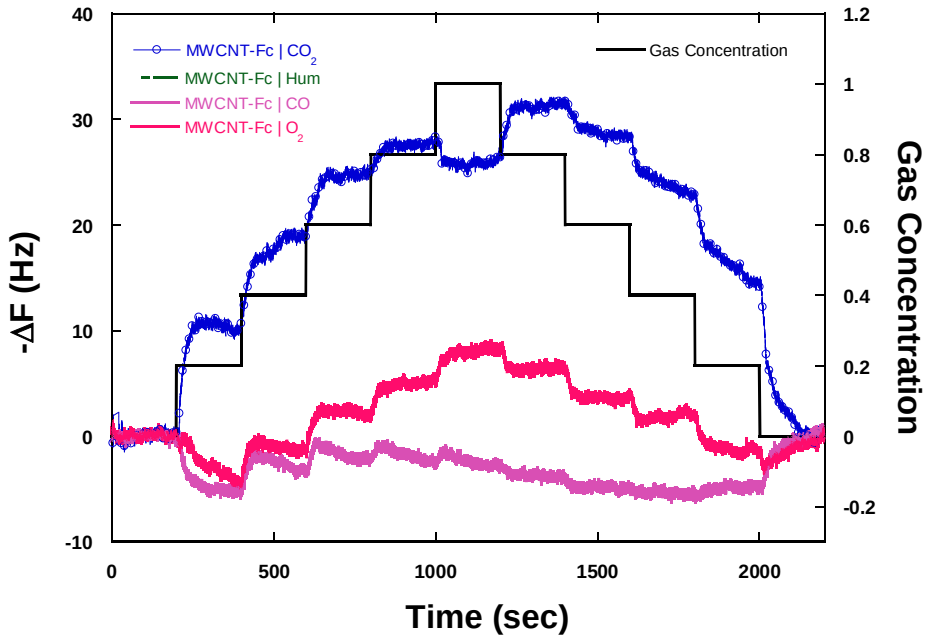

Figure 5.6. Gas responses of MWCNT-Fc thin-film coatings towards CO, CO_2, O_2 and humidity under step gas flow regime.

Figure 5.6 shows the frequency shift response of MWCNT-Fc to CO, CO_2, O_2 and humidity under step gas flow regime. Again, ferrocene modification clearly improved the sensitivity of MWCNTs, most prominently towards CO_2. Oxygen and carbon monoxide exhibited the same non-linear QCM effect in the previous measurement, whereas at the highest concentration, CO_2 showed a slight non-linear QCM behavior.

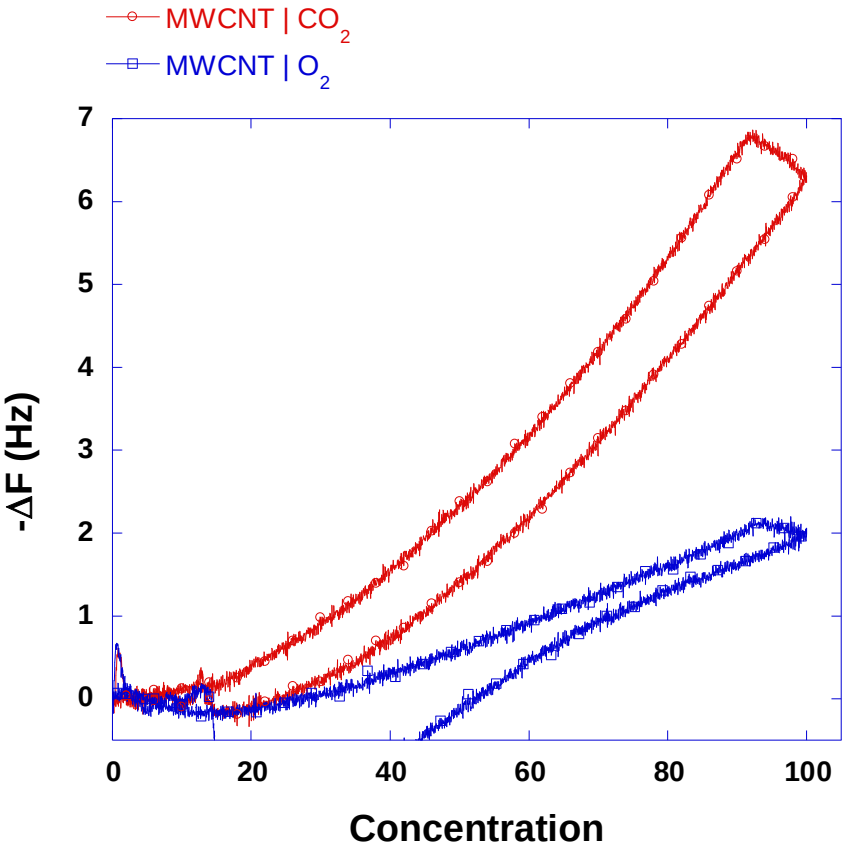

Figure 5.7. Gas responses of MWCNT thin-film coatings towards CO, CO_2, O_2 and humidity under linear gas flow regime.

Figure 5.7 shows the frequency shift response of MWCNT to CO, CO_2, O_2 and humidity under linear gas flow regime. Response of MWCNT to CO_2 is mostly linear and has a reversible character. But O_2 response was not totally reversible, which means upon the introduction of the desorption gas, the adsorbed O_2 molecules did not totally desorp from the surface and residual amounts of O_2 remained bonded on the film.

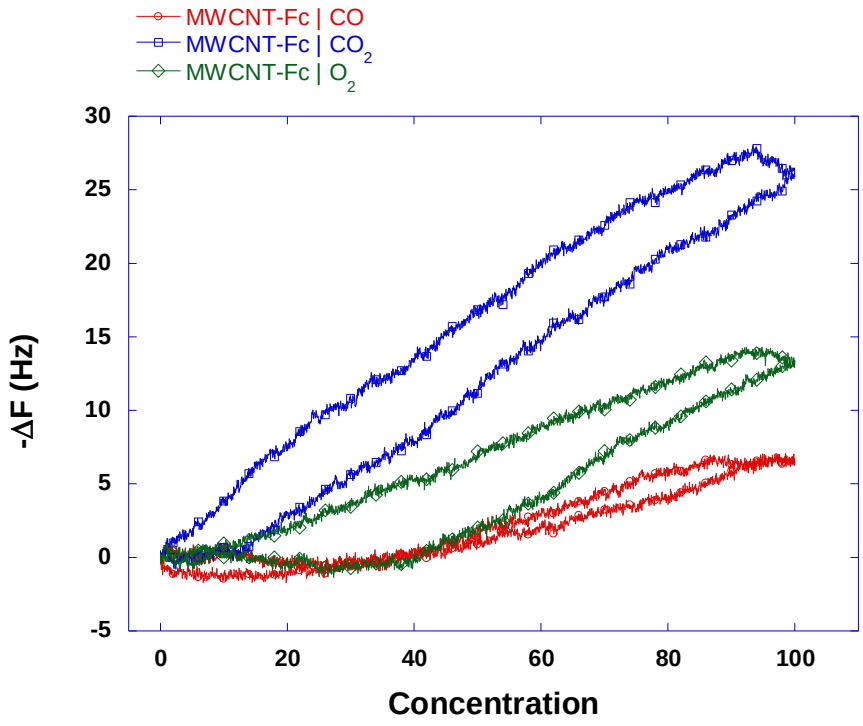

Figure 5.8. Gas responses of MWCNT-Fc thin-film coatings towards CO, CO_2, O_2 and humidity under linear gas flow regime.

Figure 5.8 shows the frequency shift response of MWCNT-Fc to CO, CO_2, O_2 and humidity under linear gas flow regime. Responses of MWCNT are mostly linear and have a reversible character.

As a consequence of the presented experimental data, the anticipated interaction mechanism of carbon nanotubes with the gases can be tied to the existence of a broad conjugated electron system in CNT structure exposing unpaired π-electrons as possible interaction sites. It can be deduced that the weak interactions of the gas molecules with MWCNT and MWCNT-Fc samples during physisorption may arise from the engagement of gas molecules' unpaired electrons with the de-localized electrons of CNTs. Ferrocene, as well, has delocalized electrons within its conjugated π-systems in both of its Cp rings. These also pose as possible interaction sites with gas molecules. But the enhancement of gas sorption ability of CNTs after Fc modification can be explained by the existence of the Fe^{2+} cation in Fc. This can corroborate to the fact that Fc modification induced sorption response towards humidity.

5.2.1.2. Gas Measurement Results of FeO/FeO-Fc Thin-Film Coatings

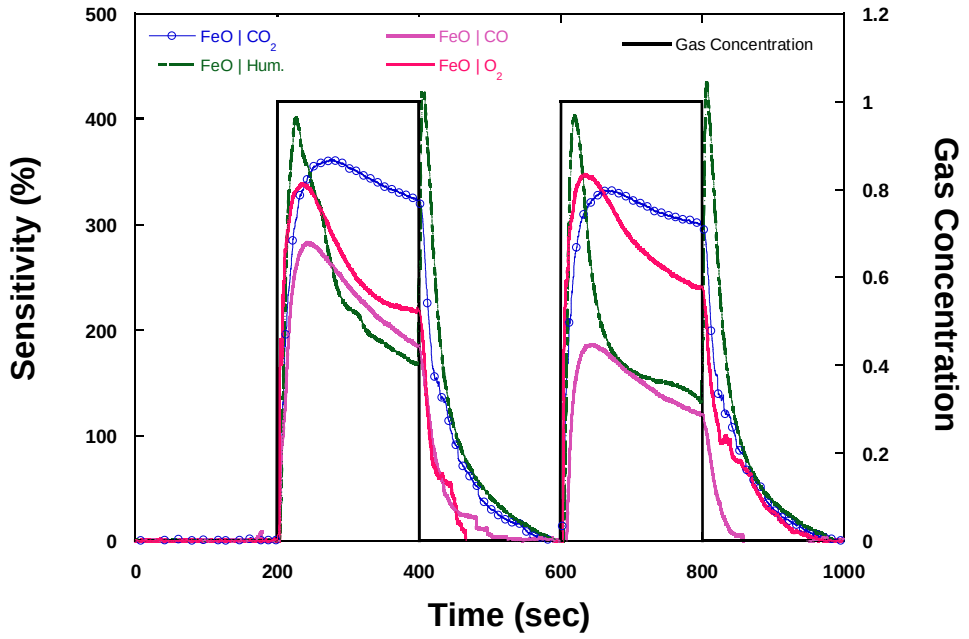

Figure 5.9. Gas responses of FeO thin-film coatings towards CO, CO2, O2 and humidity under periodic gas flow regime.

Figure 5.9 shows the sensitivity response of FeO to CO, CO_2, O_2 and humidity under periodic gas flow regime. Sensitivity values reaching 400% were attained; translating nearly 8 μg of adsorbed gas mass. This is particularly a high value, considering the mechanism of monolayer adsorption. This can mostly be attributed to the inherently large surface areas and non-stoichiometric crystalline structures of iron oxide nanoparticles, containing vacant sites, anions and cations with mixed oxidation states. These properties augment the weak interaction mechanisms responsible for physisorption of gas molecules.

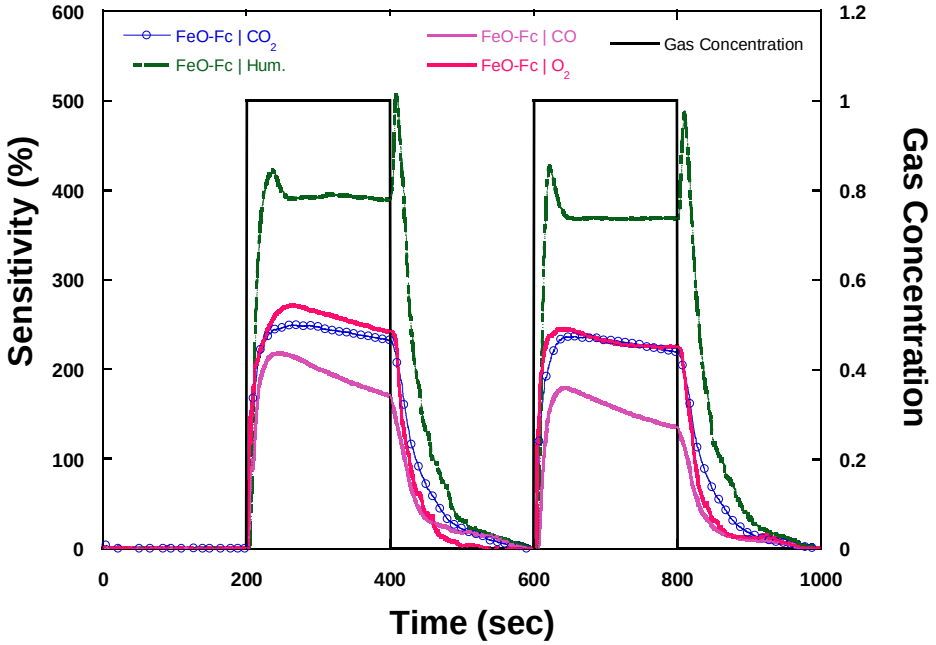

Figure 5.10. Gas responses of FeO-Fc thin-film coatings towards CO, CO_2, O_2 and humidity under periodic gas flow regime.

Figure 5.10 shows the sensitivity response of FeO-Fc to CO, CO_2, O_2 and humidity under periodic gas flow regime. Fc modification provided a slight improvement in the sensitivity values.

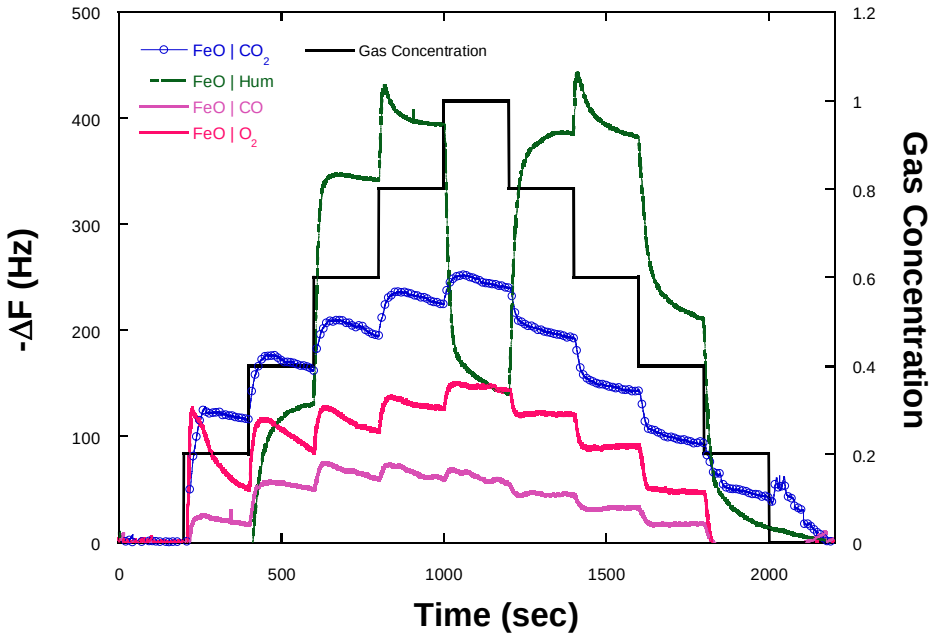

Figure 5.11. Gas responses of FeO thin-film coatings towards CO, CO_2, O_2 and humidity under step gas flow regime.

Figure 5.11 shows the frequency shift response of FeO to CO, CO_2, O_2 and humidity under step gas flow regime. Frequency shifts reminiscent of sensitivity values in the step measurements are attained again. Humidity showed a steep non-linear QCM behavior at the highest concentration which can be attributed to multilayer water molecule adsorption and viscoelastic phase formation on the thin-film surface.

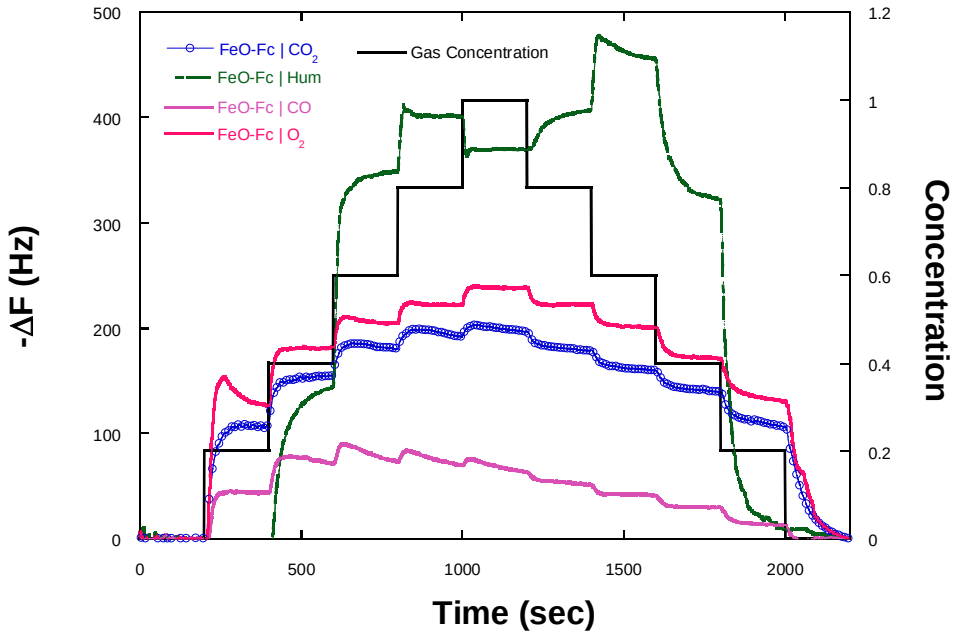

Figure 5.12. Gas responses of FeO-Fc thin-film coatings towards CO, CO_2, O_2 and humidity under step gas flow regime.

Figure 5.12 shows the frequency shift response of FeO-Fc to CO, CO_2, O_2 and humidity under step gas flow regime. Frequency shifts reminiscent of sensitivity values in the step measurements are attained again. Humidity again showed a non-linear QCM behavior but to a lesser degree.

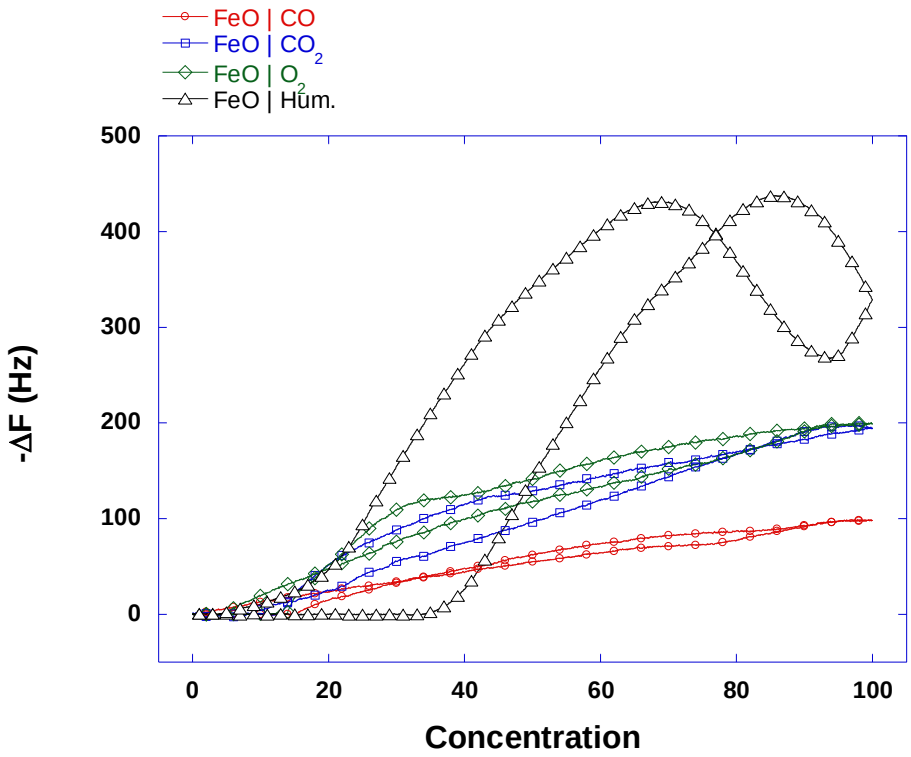

Figure 5.13. Gas responses of FeO thin-film coatings towards CO, CO_2, O_2 and humidity under linear gas flow regime.

Figure 5.13 shows the frequency shift response of FeO to CO, CO_2, O_2 and humidity under linear gas flow regime. Frequency shifts reminiscent of sensitivity values in the step measurements are attained again. Responses of FeO are mostly linear and have a reversible character. Only humidity response showed hysteresis, which is clearly attributed to the non-linear QCM behavior that was previously seen in the step measurement.

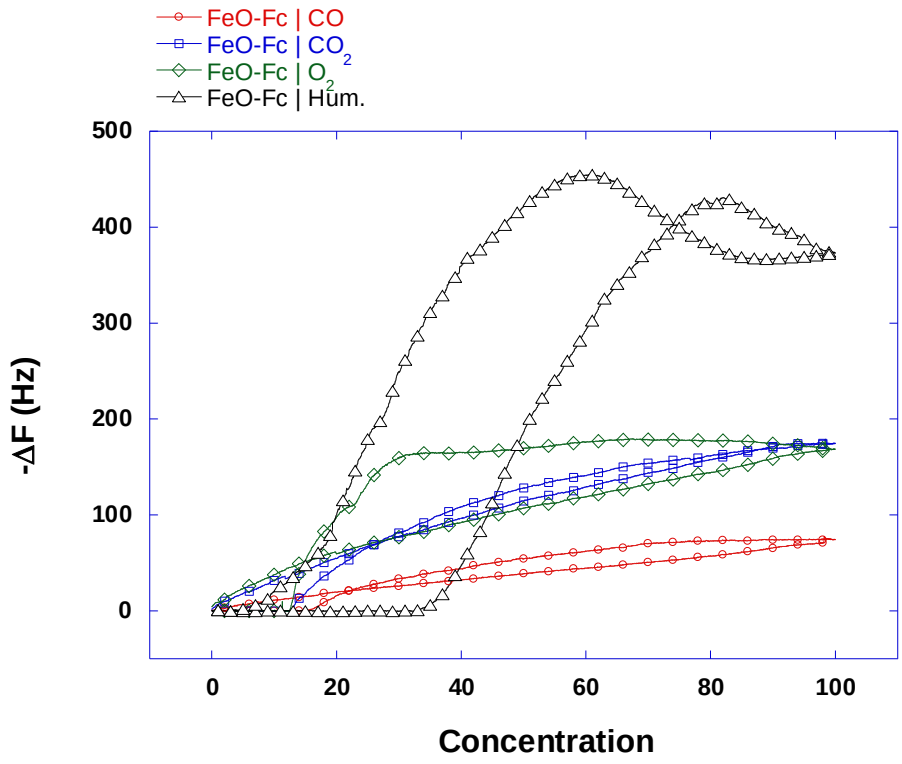

Figure 5.14. Gas responses of FeO-Fc thin-film coatings towards CO, CO_2, O_2 and humidity under linear gas flow regime.

Figure 5.14 shows the frequency shift response of FeO-Fc to CO, CO_2, O_2 and humidity under linear gas flow regime. Frequency shifts reminiscent of sensitivity values in the step measurements are attained again. Responses of FeO-Fc are mostly linear and have a reversible character. Only humidity response showed hysteresis, albeit to a lesser extent, which is clearly attributed to the non-linear QCM behavior that was previously seen in the step measurement.

The exceptionally high gas sensitivities attained by FeO and FeO-Fc samples, considering the mechanism of multilayer adsorption, can mostly be attributed to the inherently large surface areas and non-stoichiometric crystalline structures of iron oxide nanoparticles, containing vacant sites, anions and cations with mixed oxidation states.

Table 5.2 shows the maximum sensitivity values of the thin-film materials towards CO, CO_2, O_2 and humidity.

Table 5.2. Cumulative tabular data showing the maximum sensitivity values.

Sample	**Sensitivity**			
	CO	**CO_2**	**O_2**	**Humidity**
MWCNT	1,43 ‰	1,50 ‰	2,36 ‰	N/A
MWCNT-Fc	6,27 ‰	3,64 ‰	1,19 ‰	-26,12 ‰
FeO	282,42 %	361,85 %	338,42 %	438,4 %
FeO-Fc	298,3 %	371,4 %	342,6 %	505,62 %

5.3. Investigation of Gas Sensing Properties of Nanoparticles by IDE Technique

5.3.1. Gas Measurement Results of Thin-Film Coatings

Results of gas sensitivity measurements from IDE electrodes as resistance changes of the thin-film coated electrodes are presented here.

Experimental data of FeO and FeO-Fc thin-films could not be obtained due to the highly insulating character of these oxide materials at room temperature.

5.3.1.1. Gas Measurement Results of MWCNT/MWCNT-Fc Thin-Film Coatings

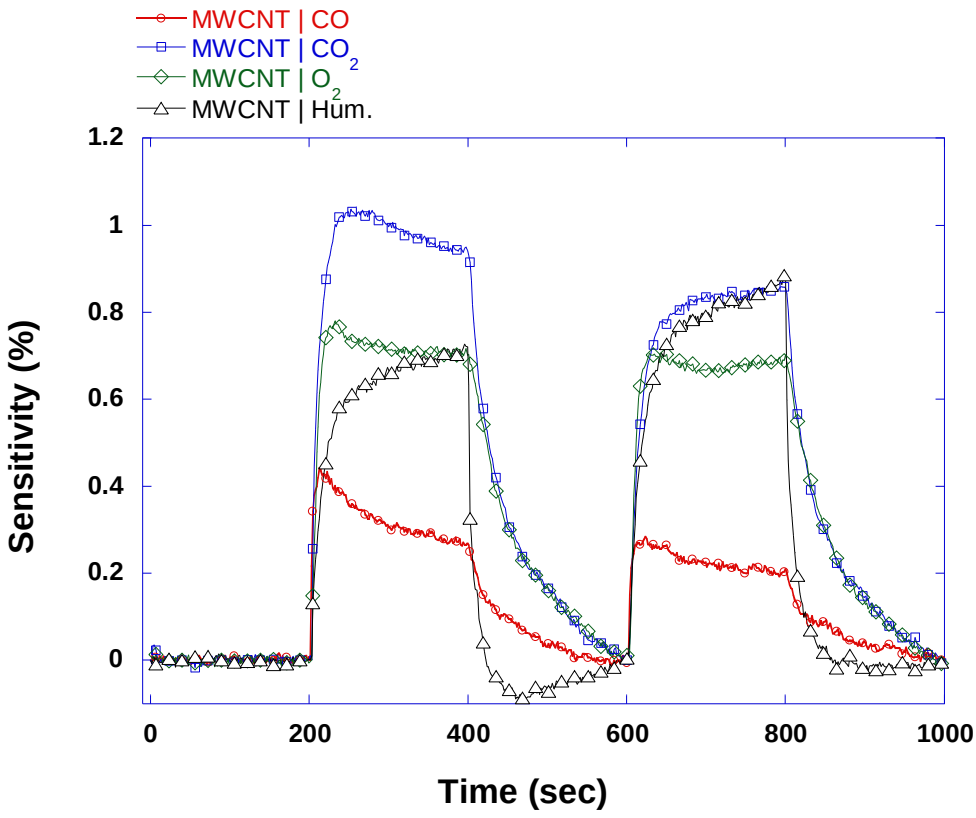

Figure 5.15. Gas responses of MWCNT thin-film coatings towards CO, CO_2, O_2 and humidity under periodic gas flow regime.

Figure 5.15 shows the sensitivity response of MWCNT to CO, CO_2, O_2 and humidity under periodic gas flow regime. It is seen that MWCNT has sensitivity towards all of the gases to varying degrees. The most prominent response of MWCNT was to CO_2 molecules, followed by O_2 and humidity.

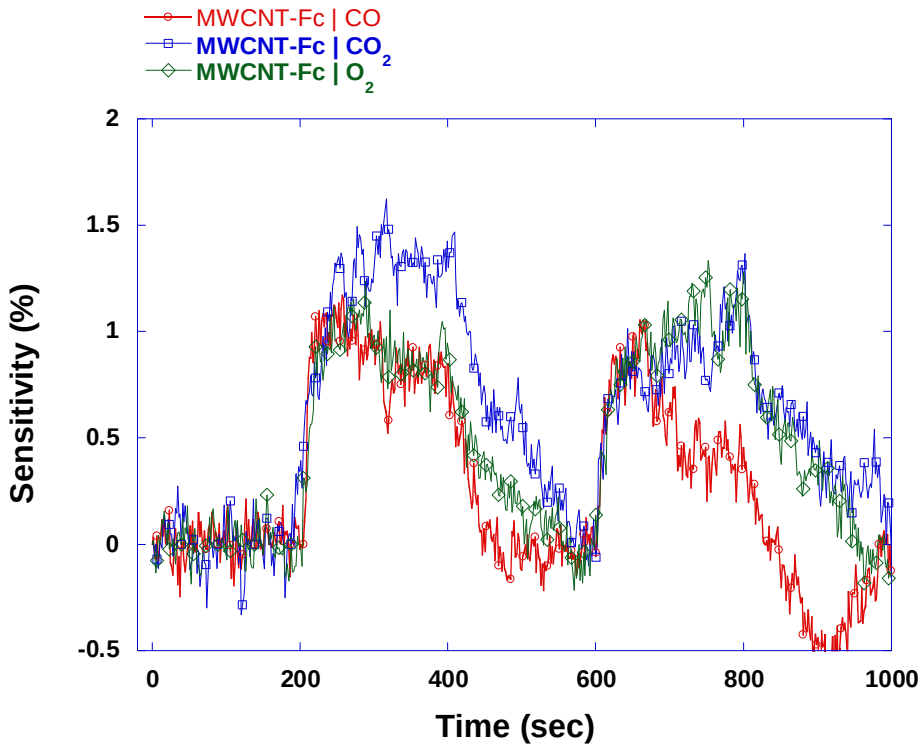

Figure 5.16. Gas responses of MWCNT-Fc thin-film coatings towards CO, CO_2, O_2 and humidity under periodic gas flow regime.

Figure 5.16 shows the sensitivity response of MWCNT-Fc to CO, CO_2, O_2 and humidity under periodic gas flow regime. Modification of conductive MWCNT with insulating Fc molecules deteriorated the electrical properties of MWCNT, yielding noisy signals. But as far as sensitivities are concerned, the results clearly show that there is not a meaningful effect of Fc modification to MWCNT to improve gas sensitivity properties of them by using IDE method to detect gases.

CHAPTER 6

CONCLUSIONS

Gas sensing properties of ferrocene functionalized multi-wall carbon nanotubes (MWCNT) and iron oxide nanoparticles were investigated via acoustic wave (QCM) and electrical based (IDE) techniques.

Considering all gas measurements were conducted at ambient temperature conditions and no activation was involved in order to induce interactions of gas molecules in the gas measurement cell with the nanoparticle thin-film coatings, such as heating the electrodes or chemically assisting the sorption processes, it can be concluded that all sorption phenomena observed throughout the gas measurement experiments are non-activated and therefore "spontaneous" process that are likely to take place at relatively low temperatures.

Consequently; physical adsorption processes responsible for the sensitivity characteristics of the nanoparticle thin-film coatings can be considered as originating from weak molecular interactions between the functional solid materials and the gas molecules, under the influence of forces known as van der Waals forces (Liu, 2012).

Carbon nanotubes have a broad conjugated electron system exposing unpaired π-electrons as possible interaction sites. It can be deduced that the weak interactions of gas molecules with MWCNT and MWCNT-Fc samples during physisorption may arise from the engagement of gas molecules' unpaired electrons with the de-localized electrons of CNTs. Ferrocene, as well, has delocalized electrons within the conjugated π-systems in both of its Cp rings. These also pose as possible interaction sites with gas molecules. But the enhancement of gas sorption ability of CNTs after Fc modification can be tied to the existence of the Fe^{2+} cation in Fc. Covalently bound iron to 2 Cp rings donates one electron to each ring transitioning to +2 oxidation state. Even though Fc is a chemically stable molecule with an 18-electron inert gas configuration, there exists a charge distribution within the molecule itself. Being a transition metal with unpaired electrons in its 3*d* shells, iron in Fc is a possible interaction site with gas molecules.

As a metal oxide having a non-stoichiometric crystalline structure containing vacant sites, anions and cations with mixed oxidation states, augmented with nanoscale size effects, iron oxide nanoparticles exhibit surface charges strongly contributing to the sensing mechanism of these materials. The exceptionally high gas sensitivities attained by FeO and FeO-Fc samples, considering the mechanism of multilayer adsorption, can mostly be attributed to the inherently large surface areas and non-stoichiometric crystalline structures of iron oxide nanoparticles, containing vacant sites, anions and cations with mixed oxidation states. Iron in the oxide nanoparticles is positioned in a non-stoichiometric crystalline lattice structure possessing various different oxidation states. Fe^{2+} cations having 4 unpaired electrons in their 3*d* shells and Fe^{3+} cations having 5 unpaired electrons in their 3*d* shells combined with oxygen vacancies provides iron an environment with a great degree of charge imbalance. These conditions confer iron oxide nanoparticles the unique properties magnifying the weak interaction mechanisms responsible for physisorption of gas molecules.

A final word on the proceedings of this study is that, even though the materials utilized in this study showed sensitivities to gases in varying degrees, harnessing them as practical gas sensors necessities the elaboration of selectivity behaviors of these materials to specific gas species. Future studies may focus on such determinations by diversifying these materials to be selective towards a specific gas molecule.

REFERENCES

Auld B. A. 1990. *Acoustic Fields and Waves in Solids*, (Krieger Publishing Company, Malabar, Florida, USA).

Arshak K., Moore E., Lyons G. M., Harris J., Clifford S. 2004. "A review of gas sensors employed in electronic nose applications", *Sensor Review*, Vol. 24, pp. 189–198.

Baleanu M. C., Nigmatullin R. R., Okur S., Ocakoglu K. 2011. "New approach for consideration of adsorption/desorption data", *Commun Nonlinear Sci Numer Simulat*. Vol. 16, pp. 4643–4648.

Ballantine D. S., White R. M., Martin S. J., Ricco A.J., Zellers E. T., Frye G. C. 1996. *Acoustic Wave Sensors: Theory, Design, & Physico-Chemical Applications*, (Academic Press, San Diego, USA).

Ballantine D. S., Wohltjen H. 1989. "Surface acoustic wave devices for chemical analysis", *Anal Chem*. Vol. 61, pp. 704–715.

Buck R. P., Lindner E., Kutner W., Inzelt G. 2004. "Piezoelectric chemical sensors", *Pure Appl. Chem*. Vol. 76, pp. 1139–1160.

Capone, S., Forleo A., Francioso L., Rella R., Siciliano P., Spadavecchia J., Presicce D. S., Taurino A. M. 2003. "Solid state gas sensors: State of the art and future activities", *J. Optoelectron. Adv. M.* Vol. 5, pp. 1335–1348.

Cheeke J. D. N., Wang Z. 1999. "Acoustic wave gas sensors", *Sens. Actuators B.* Vol. 59, pp. 146–153.

Chou, J. 2000. *Hazardous gas monitors: a practical guide to selection, operation and applications*, (McGraw-Hill, New York, USA).

Comini E., Faglia G., Sberveglieri G. 2009. *Solid State Gas Sensing*, (Springer Science & Business Media, LLC, New York, USA).

Comini E., Guidi V., Frigeri C., Ricco I., Sberveglieri G. 2001. "CO sensing properties of titanium and iron oxide nanosized thin films", *Sensors and Actuators B*. Vol. 77, pp. 16–21.

Consales M., Campopiano S., Cutolo A., Penza M. 2006. "Carbon nanotubes thin films fiber optic and acoustic VOCs sensors: Performances analysis", *Sensors and Actuators B*. Vol. 118, pp. 232–242.

Dong K-Y., Choi J., Lee Y. D., Kang B. H., Yu Y-Y., Choi H. H., Ju B.K. 2013. "Detection of a CO and NH3 gas mixture using carboxylic acid-functionalized single-walled carbon nanotubes", *Nanoscale Research Letters*. Vol. 8, pp.12.

Geim A. K., Novoselov K. S. 2007. "The rise of graphene", *Nature Materials*. Vol. 6, pp. 183–91.

Huber D. L. 2005. "Review: Synthesis, Properties, and Applications of Iron Nanoparticles", *Small*. Vol. 5, pp. 482–501.

Iijima S. 1991. "Helical microtubules of graphitic carbon", *Nature*. Vol. 354, 56–8.

Jolly W. L. 1970. *The Synthesis and Characterization of Inorganic Compounds*, (Prentice-Hall Inc, New Jersey, USA).

Kim C., Park E., Song C. K., Koo B. W. 2001. "Ferrocene end-capped dendrimer: synthesis and application to CO gas sensor", *Synthetic Materials*. Vol. 123, pp. 493–496.

King W. H. 1964. "Piezoelectric sorption detector", *Anal. Chem*. Vol. 36, pp. 1735.

Koseoglu Y., Aldemir I., Bayansal F., Kahraman S., Cetinkara H. A. 2013. "Synthesis, characterization and humidity sensing properties of $Mn_{0.2}Ni_{0.8}Fe_2O_4$ nanoparticles", *Materials Chemistry and Physics*, Vol. 139, pp. 789–793.

Langmuir I. 1916. "The constitution and fundamental properties of solids and liquids", *J Am Chem Soc*. Vol. 38, pp. 2221–95.

Laurent S., Forge D., Port M., Roch A., Robic C., Elst L. V., Muller R. N. 2008. "Magnetic Iron Oxide Nanoparticles: Synthesis, Stabilization, Vectorization, Physicochemical Characterizations, and Biological Applications", *Chem. Rev.* Vol. 108, pp. 2064–2110.

Liu X., Cheng S., Liu H., Hu S., Zhang D., Ning H. 2012. "A Survey on Gas Sensing Technology", *Sensors*. Vol. 12, pp. 9635–9665.

Neri G., Bonavita A., Galvagno S., Siciliano P., Capone S. 2002. "CO and NO_2 sensing properties of doped-Fe_2O_3 thin films prepared by LPD", *Sensors and Actuators B*. Vol. 82, pp. 40–47.

Penza M., Cassano G., Aversa P., Cusano A. 2005. "Carbon nanotubes-coated multi-transducing sensors for VOCs detection", *Sensors and Actuators B*. Vol. 111-112, pp. 171–180.

Philippova O., Barabanova A., Molchanov V., Khokhlov A. 2011. “Magnetic polymer beads: Recent trends and developments in synthetic design and applications”, *European Polymer Journal*. Vol. 47, pp. 542–559.

Potyrailo R. A., Leach A. M., Morris W. G., Gamage S. K. 2006. “Chemical sensors based on micro-machined transducers with integrated piezoresistive readout”, *Anal. Chem*. Vol. 78, pp. 5633–5638.

Reich S., Thomsen C., Maultzsch, J. 2004, *Carbon Nanotubes: Basic Concepts and Physical Properties*, (John Wiley & Sons Ltd, West Sussex, England).

Saito R., Dresselhaus M., Dresselhaus G. 1995. “Physics of carbon nanotubes”, *Physics of Carbon Nanotubes*. Vol. 33(7), pp. 883–891.

Salamonsson A., Eriksson M., Dannetun H., 2005. “Hydrogen interaction with platinum and palladium metal-insulator-semiconductor devices”, *J. Appl. Phys*. Vol. 98, pp. 014505-1–014505-9.

Sauerbrey G.Z. 1959. “The use of quartz oscillators for weighing thin layers and for microweighing”, *Z. Physik*. Vol. 155, pp. 206–222.

Si P., Mortensen J., Komolov A., Denborg J., Moller P. J., 2007. Polymer coated quartz crystal microbalance sensors for detection of volatile organic compounds in gas mixtures”, *Analytica Chimica Acta*, Vol. 597, pp. 223–230.

Stepnicka P. 2008. *Ferrocenes: Ligands, Materials and Biomolecules*, (John Wiley & Sons Ltd, West Sussex, England).

Suri K., Annapoorni S., Sarkar A. K., Tandon R. P. 2002. “Gas and humidity sensors based on iron oxide–polypyrrole nanocomposites”, *Sensors and Actuators B*. Vol. 81, pp. 277–282.

Tandon R. P., Tripathy M. R., Arora A. K., Hotchandani S. 2006. “Gas and humidity response of iron oxide–Polypyrrole nanocomposites”, *Sensors and Actuators B*. Vol. 114, pp. 768–773.

Ward M. D., Buttry D. A. 1990. “In-situ interfacial mass detection with piezoelectric transducers”, *Science*. Vol. 249, pp. 1000–1007.

Wenzel S.W., White R.M. 1989. “Analytic comparison of the sensitivities of bulk-wave, surface-wave, and flexural plate-wave ultrasonic gravimetric sensors”, *Appl. Phys. Lett*. Vol. 54, pp. 1976–1978.

Williamson K. L. 2004. *Organic Experiments Ninth Edition*, (Houghton Mifflin Company, Boston, MA, USA).

Wohltjen H., Dessy R. 1979. “Surface acoustic-wave probe for chemical-analysis. 1. Introduction and Instrument Description”, *Anal. Chem*. Vol. 51, pp.1458–1464.

Zribi A., Fortin J. 2009. *Functional Thin Films and Nanostructures for Sensors, Integrated Analytical Systems*, (Springer Science & Business Media, LLC, New York, USA).